nature cell biology

ARTICLES

https://doi.org/10.1038/s41556-019-0418-y

Haematopoietic stem cells in perisinusoidal niches are protected from ageing

Mehmet Saçma[1,12], Johannes Pospiech[1,12], Ruzhica Bogeska[2], Walter de Back[3], Jan-Philipp Mallm[4], Vadim Sakk[1], Karin Soller[1], Gina Marka[1], Angelika Vollmer[1], Rebekah Karns[5], Nina Cabezas-Wallscheid[6], Andreas Trumpp[2], Simón Méndez-Ferrer[7,8], Michael D. Milsom[2], Medhanie A. Mulaw[9], Hartmut Geiger[1,10] and Maria Carolina Florian[1,11]*

With ageing, intrinsic haematopoietic stem cell (HSC) activity decreases, resulting in impaired tissue homeostasis, reduced engraftment following transplantation and increased susceptibility to diseases. However, whether ageing also affects the HSC niche, and thereby impairs its capacity to support HSC function, is still widely debated. Here, by using in-vivo long-term label-retention assays we demonstrate that aged label-retaining HSCs, which are, in old mice, the most quiescent HSC subpopulation with the highest regenerative capacity and cellular polarity, reside predominantly in perisinusoidal niches. Furthermore, we demonstrate that sinusoidal niches are uniquely preserved in shape, morphology and number on ageing. Finally, we show that myeloablative chemotherapy can selectively disrupt aged sinusoidal niches in the long term, which is linked to the lack of recovery of endothelial Jag2 at sinusoids. Overall, our data characterize the functional alterations of the aged HSC niche and unveil that perisinusoidal niches are uniquely preserved and thereby protect HSCs from ageing.

Bone marrow (BM) HSC niches are composed of multiple haematopoietic and non-haematopoietic cells interacting in a complex three-dimensional architecture to support HSC function[1–12]. On ageing, HSC activity decreases, resulting in impaired tissue homeostasis, reduced engraftment following transplantation and increased susceptibility to diseases and leukaemia[13–18]. Changes in the HSC niche on ageing might also affect stem cell activity[19].

Here, to functionally characterize the interaction between BM niches and HSCs on ageing, we employed SCL-tTAxH2B-green flourescent protein (GFP) double heterozygous mice to identify aged HSCs that can retain the pulsed histone H2B-green fluorescent protein (H2B-GFP) label in vivo after at least 18 months of doxycycline (Dox) treatment (Fig. 1a; aged label-retaining HSCs, aLR-HSCs). LR-HSCs have been shown to act as a reserve stem cell population that resisted chemotherapeutic challenge[20–25]. We demonstrate that in aged mice LR-HSCs reside predominantly in sinusoidal niches and are functionally superior to non-LR HSCs. We show that on ageing, HSCs are located more distantly to multiple types of BM niche cells, but not from sinusoids or perisinusoidal Nestin(Nes)-GFP^{low} cells. Sinusoidal niches and Nes-GFP^{low} cells remain uniquely preserved in shape, morphology and number on ageing. We show that jagged canonical notch ligand 2 (Jag2) is expressed at sinusoids and perisinusoidal Nes-GFP^{low} cells in proximity to aLR-HSCs, and that blocking of endothelial Jag2 promotes HSC proliferation. Finally, we demonstrate that myeloablative chemotherapy disrupts the function of aged sinusoidal niches long-term, which is linked to the lack of recovery of endothelial Jag2 at sinusoids after chemotherapy, and results in haematopoietic failure and decreased survival of aged mice.

Overall, our data characterize the divergence in niche preservation of HSC function during ageing and unveil that perisinusoidal niches are uniquely protected, supporting the observation of aLR-HSCs located in their proximity. These findings underlie that physiological alterations of the BM niche on ageing impact haematopoiesis and survival, particularly in the context of specific therapeutic or chemotherapeutic interventions.

Results

aLR-HSCs are located in proximity to sinusoids. At 20 months of age, after 18 months of continuous Dox chase, 0.0057 ± 0.0013% of BM cells were LR-HSCs (gated as Lin$^-$Kit$^+$Sca-1$^+$Flk2$^-$CD34$^-$CD48$^-$CD150$^+$H2B-GFP$^+$) (Extended Data Fig. 1a–d). It should be noted that the ageing-associated expansion of LR-HSCs was relatively modest (~3-fold), compared with an ~11.8-fold expansion of aged GFP$^-$ non-LR-HSCs (anLR-HSCs) (Extended Data Fig. 1e). Based on single aLR-HSC transplantation assays into *Rag2*$^{-/-}\gamma c^{-/-}$*Kit*$^{W/Wv}$ recipient mice[26], more than 80% of these cells were functional long-term HSCs (Extended Data Fig. 1f–h). Both aLR-HSCs and anLR-HSCs were reconstituted in hosts up to secondary transplants. The population of aLR-HSCs demonstrated a more than eightfold engraftment

[1]Institute of Molecular Medicine, Stem Cells and Aging, Aging Research Center, Ulm University, Ulm, Germany. [2]Heidelberg Institute for Stem Cell Technology and Experimental Medicine gGmbH, Deutsches Krebsforschungszentrum, Division of Experimental Hematology, Heidelberg, Germany. [3]Institute for Medical Informatics and Biometry, Faculty of Medicine Carl Gustav Carus, Technische Universität Dresden, Dresden, Germany. [4]Deutsches Krebsforschungszentrum, Division of Chromatin Network, Heidelberg, Germany. [5]Division of Gastroenterology, Hepatology, and Nutrition, Cincinnati Children's Hospital Medical Center and University of Cincinnati, Cincinnati, OH, USA. [6]Max Planck Institute of Immunobiology and Epigenetics, Freiburg, Germany. [7]Wellcome Trust-Medical Research Council Cambridge Stem Cell Institute and Department of Hematology, University of Cambridge, Cambridge, United Kingdom. [8]National Health Service Blood & Transplant, Cambridge Biomedical Campus, Cambridge, United Kingdom. [9]Molecular Oncology Institute of Experimental Cancer Research, Medical Faculty, University of Ulm, Ulm, Germany. [10]Division of Experimental Hematology and Cancer Biology, Cincinnati Children's Hospital Medical Center and University of Cincinnati, Cincinnati, OH, USA. [11]Center for Regenerative Medicine in Barcelona, Bellvitge Institute for Biomedical Research, Barcelona, Spain. [12]These authors contributed equally: Mehmet Saçma, Johannes Pospiech. *e-mail: carolina.florian@uni-ulm.de

in blood and a tendency to increased reconstitution of the stem and progenitor pools as well as of all blood lineages when compared with anLR-HSC in both primary and secondary recipients (Extended Data Fig. 2a–e). The single lineages did not show significant differences between samples, despite the significant higher overall engraftment in aLR-HSC recipients. The aLR-HSCs were predominantly composed of young-like polar HSCs, whereas the anLR-HSCs were largely apolar (Extended Data Fig. 2f–i)[19,27–29]. Therefore, function and phenotypes associated with ageing characterize primarily nLR-HSCs in aged mice.

Next, we hypothesized that LR-HSCs in the aged BM might be located at selected niches, here defined as three-dimensional spatial areas of the BM tissue, characterized by presence of HSCs and selected cell types situated in proximity to each other (Fig. 1b). Young HSCs are found as individual stem cells[30] in proximity to periarteriolar and perisinusoidal cells[1–5], reside frequently at the endosteal area of the BM cavity[1,6,7] and often associate with megakaryocytes (MKs)[8–10]. Although young LR and CD150$^+$ LR cells were found homogenously throughout the BM and also at the endosteal area, in agreement with previous reports[21], aLR-HSCs were always observed as individual stem cells mostly located close ($8.1 \pm 1.2\,\mu m$) to the vasculature, $>50\,\mu m$ from the endosteum (Fig. 1c,f,g and Extended Data Fig. 3a,b). In contrast, anLR-HSCs were found more frequently in clusters[30,31] and were located significantly further from the vasculature (at $18.5 \pm 1.2\,\mu m$ and $21.7 \pm 1.0\,\mu m$, for single and clustered anLR-HSCs, respectively; see Fig. 1d–g). The aLR-HSCs were found almost exclusively (83%) located in proximity to sinusoids, whereas only 19% and 10% of single and clustered anLR-HSCs, respectively, were found at sinusoids (Fig. 1h–j, Supplementary Video 1 and Extended Data Fig. 3c–f for the histological distinction between sinusoidal and arteriolar vessels). The aLR-HSCs and anLR-HSCs were not located in proximity to either the endosteum or MKs (Fig. 1k–m). Therefore, aLR-HSCs are individual stem cells found selectively and specifically in proximity to perisinusoidal niches.

Aged HSCs are located distant to most niche cells but close to perivascular Nes-GFP^{low} cells and sinusoids. Intrigued by our findings on aLR-HSCs, we performed a more comprehensive characterization to see if the distance of HSCs from niche cells changes with ageing. In the BM endosteal region of young mice, HSC frequency was more than twofold higher compared with aged mice, and HSCs were significantly more distant from the endosteum (Fig. 2a–d, Extended Data Fig. 4a and Supplementary Table 1). Aged HSC frequencies were comparable between histology and flourescence-activated cell sorting (FACS) analyses (Supplementary Table 2). As previously reported[8,10], $26 \pm 2\%$ of HSCs in the young BM were in proximity to MKs, while in the aged setting, only $10.3 \pm 2.1\%$ of HSCs were located near to MKs (Extended Data Fig. 4b–e). In aged mice, the frequency of HSCs in proximity to Nes-GFP^{high} cells was also significantly reduced, while the frequency of HSCs adjacent to Nes-GFP^{low} cells was unaltered. Therefore, the mean distance of HSCs to the nearest Nes-GFP^{high} cell was increased in aged BM, whereas the mean distance to the nearest Nes-GFP^{low} cell was unchanged (Fig. 2e and Extended Data Fig. 4f–k). Most Nes-GFP^{low} cells were Leptin receptor$^+$ (LepR$^+$), and the distance of HSCs to perisinusoidal LepR$^+$ cells in young and aged BM was similar (Extended Data Fig. 5a–d). Still, we have to consider that the antibody staining is not labelling the long processes of LepR$^+$ cells; therefore these data may underestimate the distance of HSCs to LepR$^+$ cells, particularly to LepR$^+$ cell processes, as reported elsewhere[3]. Furthermore, HSCs were located equally distant to the vasculature in young and aged BM, while HSCs in aged mice were more distant from arterioles but not from sinusoids (Fig. 2f,g, Extended Data Fig. 5e–g and Supplementary Videos 2–5). The frequency and localisation of Ki67$^+$ HSCs in young and aged BM was comparable (Extended Data Fig. 5h–i and Supplementary Table 3). Thus, HSCs in aged BM lose proximity to multiple niche cells but not to sinusoids and perisinusoidal Nes-GFP^{low} cells.

Next, we investigated the extent to which ageing alters the number and the architecture of the different niche cells. In both central and endosteal BM preparations[7,12], Nes-GFP^{high} cells were significantly decreased on ageing, while the frequency of Nes-GFP^{low} cells remained similar (Fig. 3a–d and Extended Data Fig. 5j). The number of MKs was increased (Fig. 3e,f and Extended Data Fig. 6a,b). The frequency of endothelial cells (ECs) in the endosteal area was significantly decreased, although the overall vasculature volume and the endothelial area occupancy was not altered (Fig. 3g–j and Extended Data Fig. 6c–d). Interestingly, the aged epiphyseal/metaphyseal BM vasculature, which mainly comprises arteries and arterioles[32], presented with a decreased length and diameter and a disorganized orientation of the vessels in aged BM (Fig. 3k–n). The aged BM diaphyseal area, which is located in the central bone and harbours the vast majority of the sinusoidal vessels[32,33], was not altered in diameter, length or orientation of vessels (Fig. 2k,o,q). Therefore, sinusoidal/Nes-GFP^{low} cells in aged animals, which harbour LR-HSCs (Fig. 1h), are selectively not altered with respect to architecture and number on ageing.

HSC proximity to selected niche cells is not random and endothelial Jag2 maintains aged LR-HSCs at sinusoids. We performed in silico modelling to investigate the relationship between changes in niche structure and the decreased HSC proximity on ageing. First, we simulated the distribution of 10,000 HSCs randomly placed within the BM cavity, and calculated the distance between these randomly placed cells and the different niche structures (indicated as 'expected' or 'in silico' samples) (Fig. 4a). The position of the HSCs was randomly simulated on the basis of each specific niche

Fig. 1 | Aged LR-HSCs are located in proximity to sinusoids. a, SCL-tTAxH2B-GFP mice were treated with Dox for 18 months starting at 8 weeks of age. The H2B-GFP label signal is diluted by division and over time; only dormant, rarely dividing cells retain the label. **b**, HSCs were considered in proximity to a niche cell when the distance from the centroid of a HSC to the edge of a niche cell body was less than 10 µm. The HSC radius was found to be 5 µm and the smallest non-erythroblast BM cell radius was >5 µm. **c–e**, Representative confocal whole-mount images of old SCL-tTAxH2B-GFP BM areas showing a single GFP$^+$CD150$^+$CD41$^-$CD48$^-$Lin$^-$ LR-HSC (**c**), a single GFP$^-$CD150$^+$CD41$^-$CD48$^-$Lin$^-$ nLR-HSC (**d**) and clustered nLR-HSCs (**e**) (arrowheads). LR-HSCs that were observed to maintain H2B-GFP$^+$ nuclei are shown in green; FABP4$^+$ vasculature is shown in magenta. HSCs that are CD150$^+$ are shown in red, and those negative for the other haematopoietic markers (CD41, CD48 and lineage) are in grey. **f**, The percentages of single and clustered nLR-HSCs and LR-HSCs. **g**, The mean distances of single LR-HSCs and single and clustered nLR-HSCs to the nearest vasculature. **h**, The percentages of single LR-HSCs, single and clustered nLR-HSCs in proximity (<10 µm) to sinusoids (83.33%, 19.08% and 9.46%, respectively), arterioles/arteries (5.56%, 9.21% and 0.00%, respectively) and MKs (27.78%, 19.33% and 5.33%, respectively). **i**, Three-dimensional reconstructed images of old SCL-tTAxH2B-GFP BM showing a LR-HSC (arrowhead) in proximity to sinusoidal vasculature. **j**, The percentages of different HSC types that are adjacent to sinusoids (<10 µm, 29%, 57% and 14%, respectively). **k**, The mean distances of single LR-HSCs and single and clustered nLR-HSCs to the nearest endosteum. **l**, The mean distances of single LR-HSCs and single and clustered nLR-HSCs to the nearest MK. **m**, LR-HSC (arrowhead) in proximity to a MK. Experiments in **c–e**, **i** and **m** were repeated independently 7 times with similar results. Data in **f–h** and **j–l** was obtained from $n = 245$ total HSCs from 6 mice, from 51 longitudinal humeral and femoral cross-section areas, and from 7 biological repeats. Data represent the mean ± s.e.m. In **g**, **k** and **l** the statistical significance was assessed by a two-tailed Mann–Whitney-test. Scale bars, 20 µm. See also Extended Data Figs. 1–2, Supplementary Video 1 and Source Data Fig. 1.

structure (see Supplementary Fig. 1 and Methods for additional experimental details). Second, we compared the simulated random distributions (expected) with our three-dimensional histological data. Based on this analysis, we could conclude that the localisation of HSCs is not random in both young and aged BM with respect to all the selected niche cells (Fig. 4b and Extended Data Fig. 6e–g).

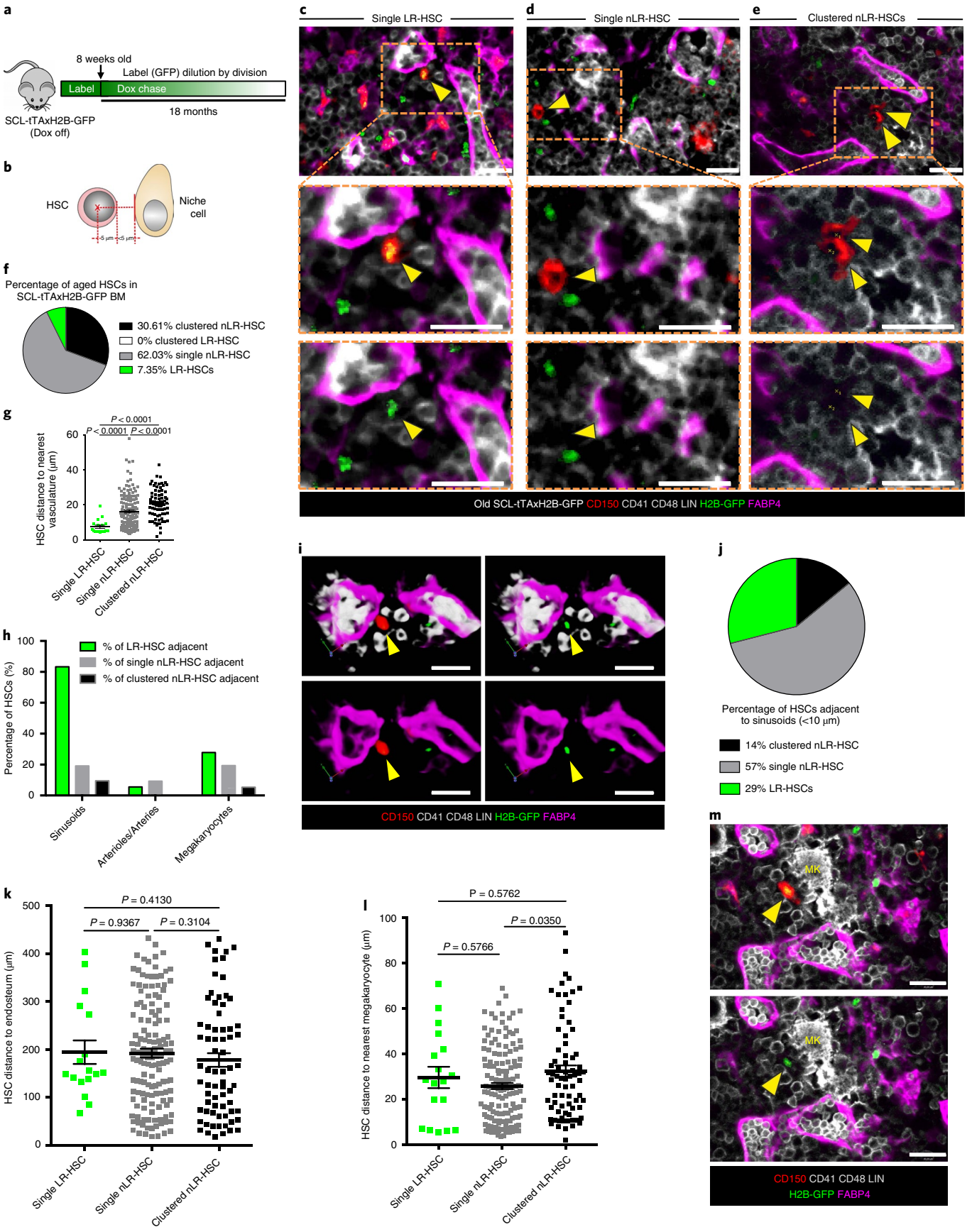

Next, we compared differences between young and aged samples. First, we analysed the changes in distances between the samples generated computationally (in silico). Therefore, we compared the in silico young and aged samples side by side for each niche structure to calculate the expected difference. In a similar way, we examined the histological measurements from young and aged samples side by side for each niche structure, to quantify the 'observed' difference (Fig. 4c). Finally, we correlated the in silico expected results (young versus aged) with the histological observed results (young versus aged) (Fig. 4d). The data ultimately revealed that the increase in the in silico predicted distance of HSCs from Nes-GFP^{high} cells, and from the endosteum, agrees with the histological data, suggesting that the change in HSC distance might be linked to the systematic changes in structure and/or distribution of these niche cells, which was expected based on the sole structural change of these niche cells with ageing (Fig. 4c,d and Extended Data Fig. 6h). Both the in silico model and the histological data indicated that the distance from Nes-GFP^{low} cells was not altered (Fig. 4d and Extended Data Fig. 6i). With regards to MKs, the model did not predict changes with ageing, indicating that the observed increased distance is not driven by changes in MK distribution (Fig. 4d and Extended Data Fig. 6j).

To further validate the relevance of the HSC position with respect to niche cells, we assessed whether we could predict whether a HSC is young or aged, based on the relative distance to various niche cells. To this end, we performed a keras/tensorFlow multilayer deep learning analysis based on the seven different distance measurements of HSCs from vasculature, endosteum, NesGFP^{low}, NesGFP^{high}, MKs andLepR^{+}, as well as the distance between individual HSCs. Alhough each histological measurement was collected from hundreds of cells, not all measurements were done simultaneously for a given cell. To address this in a robust and multivariate manner, we subsampled data from each measurement and merged them into a matrix for every training step of the model (see Methods for further details). The model was then sequentially trained for 50 rounds (iterations), with each iteration (50 epochs) taking new sampling data of the training set. Validation was done on a subset of data not seen by the model. We observed close to 70% prediction accuracy in the first iteration, which linearly increased to 82.5% after 50 rounds of iteration (Fig. 4e,f). To assess the model improvement efficiency with every round of subsampling, we binned the results into 10 groups (each with five iterations). A correlation analysis between the median accuracy of the bins and their ordered/ranked version (smallest to largest) was statistically highly significant, indicating that the model significantly and linearly improved over the iterations considered (Fig. 4e). When we assessed the confusion table (degree of match between empirical and predicted HSCs), we saw that the model was predicting equally well whether a HSC was young or aged, and the rate of misclassification in the validation set was comparable (14.8% of mis-classified young HSCs and 18.8% of misclassified aged HSCs; Fig. 4f). In the final step, we looked at the overall relevance of each niche cell type in the prediction analysis. All parameters were positively correlated, and there was no significant difference between their correlation coefficients (Fig. 4g), indicating that none of the niche cells are individually important, but rather that they need to be considered simultaneously (Fig. 4g and Supplementary Fig. 2). Therefore, according to our deep learning approach, the proximity of selected niche cells to HSCs can be used to predict whether a given stem cell is young or old.

To further support proximity to specific cell types as a critical aspect in characterizing whether young and aged niches are functionally different, we performed competitive young and aged HSC transplants into non-irradiated young and aged *Rag2*$^{-/-}$*γc*$^{-/-}$*Kit*$^{W/Wv}$ recipient mice (Fig. 4h). The histological and PB data showed that in young recipients, young and aged HSCs localise with significantly different frequency in proximity to the arterioles or endosteum compared with sinusoids, whereas in aged recipients, both young and aged HSCs localise with the same frequency at sinusoids (Fig. 4i–k and Extended Data Fig. 7a–f). Despite the intrinsic difference, both young and aged HSCs function as stem cells (Extended Data Fig. 7g–h). Therefore, the data substantiate the in silico model, showing that HSC proximity to selected niche cells is not random, and, at least in young mice, young and aged HSCs are found in different functional niches. In addition, the data indicate that in aged mice the endosteal/arteriolar niche is functionally disadvantaged compared with the sinusoidal niche.

Next, we performed single-cell RNA sequencing (scRNA-seq) on aLR-HSCs, which locate almost exclusively at sinusoids (Fig. 1h and Extended Data Fig. 7i). Similar to our functional data, when analysed together with scRNA-seq dataset from young HSCs[23], LR-HSCs from aged mice were transcriptionally younger than nLR-HSCs (Fig. 5a). In general, scRNA-seq precludes the identification of low abundancy transcripts, as, for example, non-canonical Wnt5a mRNA, which we reported previously to be increased in aged HSCs, and here was not detectable in both aLR-HSCs and anLR-HSCs[27]. Nevertheless, a total of 1,058 genes were significantly up regulated in aLR-HSCs compared with anLR-HSCs, including *Cxcr4*[34,35], *Dek*[36], *Gpr56*[37,38] and *Ctnnb1/β-catenin* (Fig. 5b and Extended Data Fig. 7j–o and Supplementary Table 4). Consistently, gene ontology (GO) analyses revealed an enrichment for canonical Wnt and cell polarity establishment[27], which are associated with young HSCs[28,30], despite the fact that we were not able to detect deregulation of Wnt5a in anLR-HSCs (Fig. 5c). We also observed increased expression of *Rbpj* and *Hes1*, critically linked to canonical Notch signalling[39–41] (Fig. 5d). Notch signalling in HSCs is engaged by Jag/Dll ligands on juxtaposed cells and requires cell proximity[42]. Supporting that active Notch signalling might be critical for LR-HSCs proximity at sinusoidal niches, we observed high levels of Jag2 at sinusoids and Nes-GFP^{low} cells in young, but especially aged, BM, as well as at sinusoids that were in proximity to aLR cells (Fig. 5e and Supplementary Video 6). Jag2 levels were markedly reduced

Fig. 2 | Aged HSCs are located more distant to most niche cells, but not to Nes-GFP^{low} cells and sinusoids. a,**b**, Representative three-dimensional confocal whole-mount images of longitudinally shaved C57BL/6 wild-type (WT) young (**a**) and old (**b**) femurs, showing CD150^{+} HSCs in red and CD41^{-}CD48^{-}Lin^{-} HSCs in white, both in the endosteal area. Vasculature was stained intravenously with anti-PECAM1 and anti-VE-Cadherin (CD31 and CD144, shown in blue) antibodies. Dashed lines denote the endosteum and yellow arrows show HSCs. **c**, The percentage of HSCs in the young and old femoral endosteal area (<50 μm), $n = 6$ mice per group. **d**, The mean distance of HSCs to the young and old femoral endosteum ($n = 232$ young HSCs from 56 areas and $n = 494$ aged HSCs from 30 areas, pooled from 6 mice per group). **e**, The percentage of young and aged HSCs in direct contact with Nes-GFP^{low} cells (<10 μm) (94 young HSCs and 135 aged HSCs from 7 areas, $n = 3$ mice per group). **f**, Three-dimensional confocal whole-mount images of young and old femoral WT BM. Arrowheads show arterioles, arrows HSCs. The percentage of young and aged HSCs adjacent to arterioles (<10 μm) is also given. **g**, Three-dimensional confocal whole-mount images of young and old femoral WT BM showing the spatial relationship of HSCs (arrows) and sinusoids, shown in blue. The percentage of young and old HSCs adjacent to sinusoids (<10 μm) is also shown. (**f**,**g**, 194 young HSCs from 39 areas and 397 aged HSCs from 17 areas, $n = 3$ mice per group). Data represent the mean ± s.e.m. The experiments in **a** and **b** were performed independently 7 times with similar results. In **d** the statistical significance was assessed using a two-tailed Mann–Whitney-test; in **c**, **e**, **f**, **g** statistical significance was calculated using two-tailed unpaired *t*-tests. Scale bars, 50 μm (**a**,**b**); 20 μm (**f**,**g**). See also Extended Data Figs. 3–5, Supplementary Table 1–2, Supplementary Video 2–5 and Source Data Fig. 2.

in aged Nes-GFP^{high}/arteriolar cells in aged mice (Fig. 5f). Flow cytometry analyses revealed that the frequency of Jag2^{+}Nes-GFP^{low} and Jag2^{+}ECs was preserved in aged mice, while there was a more than two-fold decrease in the frequency of Jag2^{+}Nes-GFP^{high} cells. The maintenance of Jag2 expression in sinusoids on ageing was specific to Jag2. For example, Jag1 was found to be significantly reduced

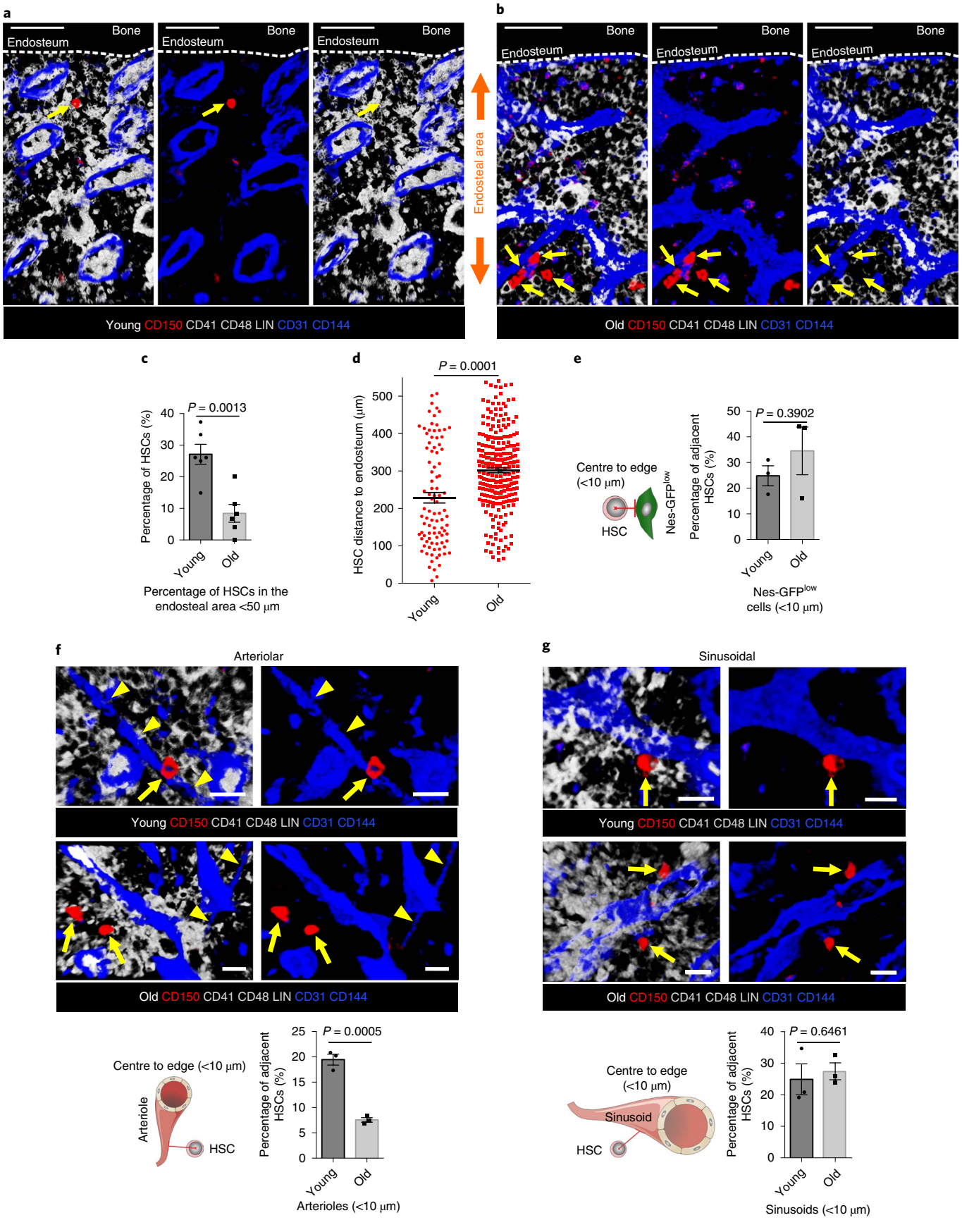

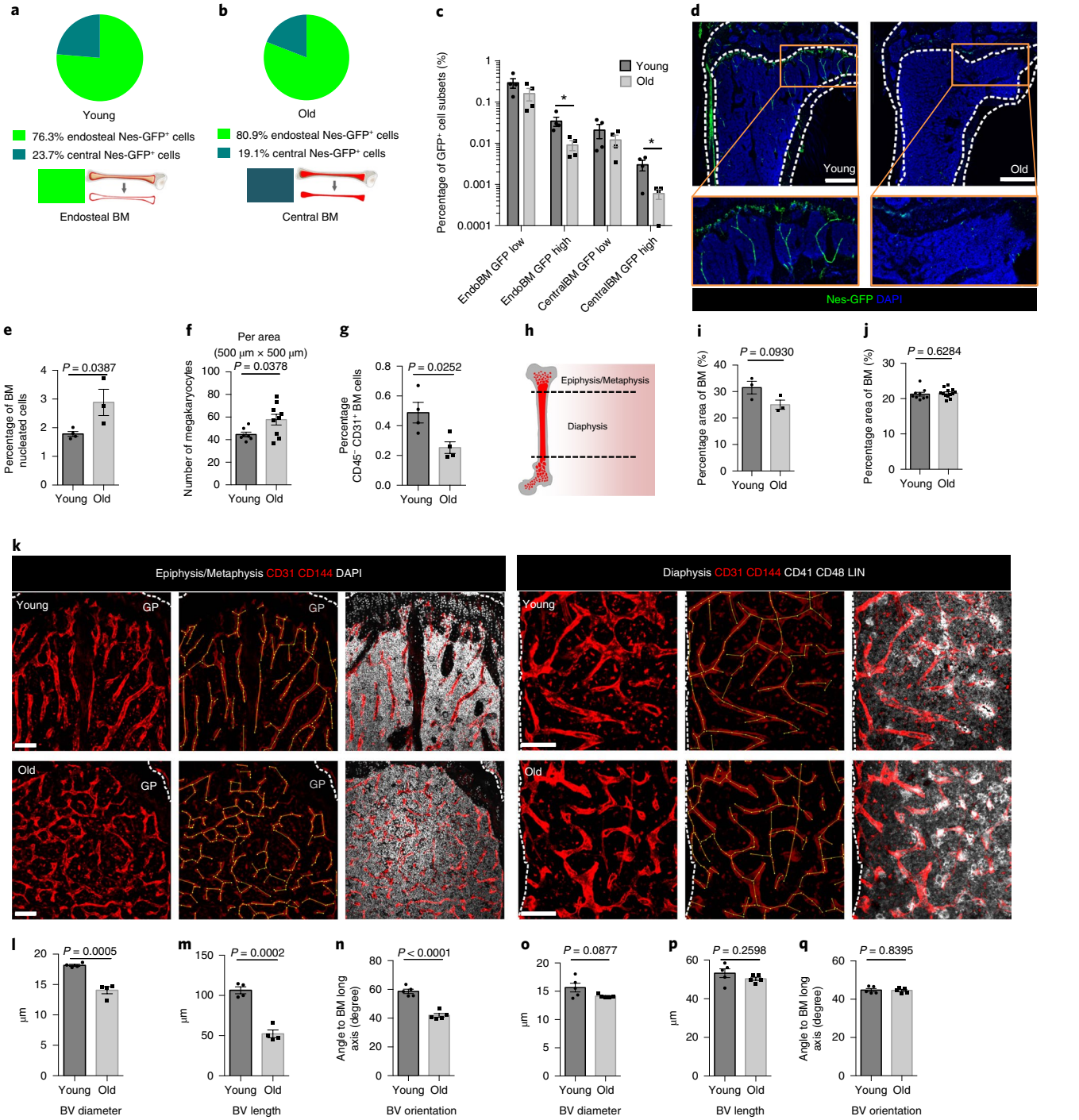

Fig. 3 | Nes-GFP^{low} cells and sinusoids are uniquely preserved on ageing. a,**b**, Pie charts depicting percentages of endosteal and central BM CD45$^-$CD31$^-$Nes-GFP$^+$ cells isolated from young (**a**) and old (**b**) Nes-GFP mice. **c**, The frequency of CD45$^-$CD31$^-$Nes-GFP^{high} and Nes-GFP^{low} cells among nucleated cells from endosteal and central BM from young and old bones from Nes-GFP mice ($n=4$ mice per group). **d**, Representative tile scanned and stacked whole-mount images of tibiae from young and old Nes-GFP mice. DAPI, 4′,6-diamidino-2-phenylindole. **e**, Frequency of CD41$^+$FSC^{high} MKs from young and old WT BM ($n=4$ young and $n=3$ old mice per group). **f**, Quantification of CD41$^+$ MKs in *z*-stacked whole-mount images acquired from young and old long bones ($n=7$ young and $n=9$ old longitudinal shaved cross-section areas, two mice per group). **g**, Frequency of CD45$^-$CD31$^+$ endothelial cells (ECs) from young and old WT endosteal BM ($n=4$ mice per group). **h**, Schematic of a long bone showing epiphysis/metaphysis and diaphysis. **i**,**j**, Epiphyseal/metaphyseal (**i**) and diaphyseal (**j**) BM areas occupied by vasculature in young and old long bones (**i**, $n=3$ areas per group from 3 mice; **j**, young $n=9$ and old $n=13$ areas, 3 mice per group). **k**, Whole-mount images showing vasculature (red) in tibial epiphysis/metaphysis and diaphysis from young and old mice. **l**–**q**, Quantification of epiphyseal/metaphyseal (**l**–**n**) and diaphyseal (**o**–**q**) blood vessel (BV) diameter, length and orientation to the bone long axis (**l**, **m**, 96 young and 293 old BVs from $n=4$ epiphyseal areas per group, from two mice per group; **n**, 96 young and 293 old BVs from $n=5$ epiphyseal areas per group, from two mice per group; **o**–**q**, 296 young and 418 old BVs from $n=5$ diaphyseal areas per group, from two mice per group). Data represent the mean ± s.e.m. Experiments in **d** and **k** were performed independently 3 times with similar results. In **c**, the statistical significance was assessed using a two-way ANOVA, and in **e**–**g**, **i**, **j** and **l**–**q** using a two-tailed unpaired *t*-test. Scale bars, 500 µm (**d**); 100 µm (**k**). See also Extended Data Figs. 5,6 and Source Data Fig. 3.

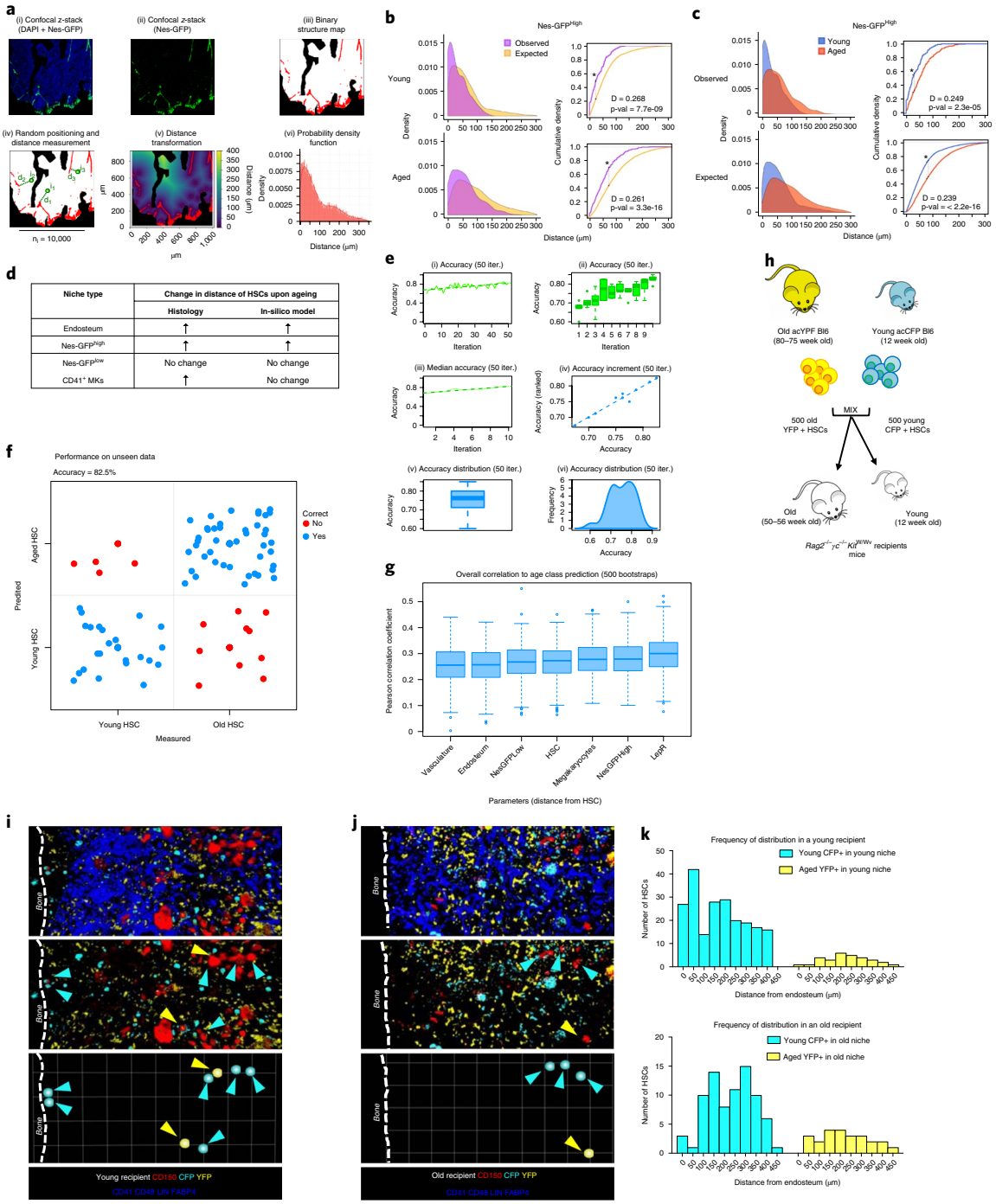

Fig. 4 | HSC proximity to selected niche cells is not random. a, Example binary structure maps and simulation process: (i) confocal *z*-stack raw image; (ii) selection of the relevant structure; (iii) signal thresholding and size selection filters applied; (iv) Euclidean distance calculation; (v) distance transformation; (vi) probability density distribution (scale bar, 200 µm). **b**, Observed (histology) versus expected (in silico) distances of HSCs from NesGFP^{high} cells in young and old mice. **c**, Young versus old HSC distances from the NesGFP^{high} cells in the observed (histology) and expected (in silico) dataset. For **b** and **c**, the two-sample Kolmogorov–Smirnov test was used to analyse the data; alpha levels were selected to control for sample sizes. $n = 137/275$ for observed young/old mice; $n = 10{,}000$ for expected young/old mice. **d**, Summary as predicted by the computational model. **e**, Keras/TensorFlow deep learning analysis. (i) alidation prediction accuracy (*y* axis) over 50 iterations (*x* axis); (ii) prediction accuracy after summarizing the 50 iterations (5 iterations per bin); median accuracy of the 10 groups (the dotted line depicts a fitted linear model); (iii) median accuracy plotted against a sorted/ranked version (the dotted line shows a linear model); (iv) overall accuracy; (v) frequency distribution of the validation accuracy. **f**, Confusion matrix: blue and red dots are correctly and misclassified HSCs, respectively. Measured (*x* axis) represents empirical data; predicted (*y* axis) represents data according to the deep learning model. **g**, Pearson correlation showing no significant difference between the parameters ($n = 500$ for each parameter). **h**, Competitive transplantation of young CFP$^+$ and aged YFP$^+$ HSCs into young and aged *Rag2*$^{-/-}$*γc*$^{-/-}$*Kit*$^{W/Wv}$ recipient mice. **i**,**j**, Representative pictures of femurs from young (**i**) and aged (**j**) recipient mice (**i**, 1 unit = 45.23 µm; **j**,1 unit = 45.72 µm). **k**, The relative distribution of donor HSCs to the endosteum in bones of young and old recipients (upper panel: $n = 212$ CFP$^+$ young and $n = 30$ YFP$^+$ aged HSCs from 31 areas, 3 mice per group; lower panel: $n = 79$ CFP$^+$ young and $n = 24$ YFP$^+$ aged HSCs from 30 areas HSCs, 3 mice per group). See also Extended Data Figs. 6, 7, Supplementary Figures 1–2 and Source Data Fig. 4.

in aged sinusoids and endothelium (Fig. 5g–i and Extended Data Fig. 8a–b). Dll1 and Dll4 were barely detectable and not changed with ageing (Fig. 5g–i). To determine the role of endothelial Jag2 for HSC function, we first performed in vitro co-culture experiments. Blocking endothelial-derived Jag2 markedly increased the number and thus proliferation of HSCs (Extended Data Fig. 8c–f). Second, we injected the Jag2-blocking antibody directly into aged mice (Fig. 5j). In BM, the Jag2-blocking antibody showed a very specific staining pattern similar to the Jag2 distribution detected by histology and flow cytometry analysis, binding mainly aged endothelial sinusoids (Extended Data Fig. 8g). Consistently with the in vitro data, blocking Jag2 in vivo induced increased proliferation of aged HSCs and clustering at sinusoids in the diaphyseal central BM (Fig. 5k–n and Extended Data Fig. 8h). Overall, in this region, the frequency of sinusoidal Ki67$^+$ HSCs doubled (Fig. 5m and Extended Data Fig. 8i–j) and the effect was almost exclusively localised at sinusoids (Extended Data Fig. 8i–k), resulting in a significant increase in the frequency of clustered HSCs in proximity to sinusoidal niches (Extended Data Fig. 8k), which are normally extremely rare in control condition. In summary, our data show that Jag2 is expressed at sinusoids and by Nes-GFP^{low} cells in aged BM in proximity to aLR-HSCs, and that endothelial Jag2 suppresses HSC proliferation and clustering.

5-fluorouracil treatment specifically disrupts sinusoidal niches and impairs haematopoiesis and survival of aged mice. To functionally investigate the sinusoidal niche in aged animals, we performed treatments with 5-fluorouracil (5-FU), which, in young mice, results in damage to sinusoidal niches as well as myelosuppression[43–45]. The aged sinusoidal niche was also considerably compromised by 5-FU, with markedly reduced cellularity and increased diameter of the sinusoidal vessels (Extended Data Fig. 9a and Fig. 6a–d). However, the arterioles and the endosteal niche were largely unaffected by 5-FU, particularly so in the case of aged mice (Fig. 6d–f). The sinusoidal disruption correlated with a reduction in Nes-GFP^{low} cells in the aged mice only, whereas Nes-GFP^{high} cells remained unaltered after 5-FU treatment (Fig. 6g,h). The percentage of cycling HSCs after 5-FU treatment remained very low in aged mice, and we did not observe clusters of proliferative multipotent progenitors (MPPs). In contrast, 61.5% of HSCs in young 5-FU treated mice were actively cycling (Ki-67$^+$), and we detected numerous clusters of proliferating MPPs. Of note, HSCs from aged mice transplanted into a young niche showed an increase in the frequency of Ki-67$^+$ HSCs after 5-FU, supporting a critical and dominant role of the young niche for the activation of HSCs after myelosuppression (Fig. 7a,b and Extended Data Fig. 9b–c). Although haematopoiesis recovered within 30 d of 5-FU treatment, after four to five months, aged 5-FU-treated mice showed a significant decrease in white blood cells associated with a reduction in long-term survival post-treatment, suggesting that the HSC compartment may be compromised (Fig. 7c,d and Extended Data Fig. 9d). To exclude the possibility that 5-FU might directly damage the HSCs, we performed transplantations of young and aged recipient mice preconditioned by 5-FU. We detected very low or absent engraftment in 5-FU preconditioned young and aged mice, whereas irradiated recipients (11 Gy) were efficiently engrafted. These data indicate that endogenous HSCs in 5-FU preconditioned recipients were not directly affected by the chemotherapy (Fig. 7e and Extended Data Fig. 9e–f). Of note, sinusoids remained significantly enlarged in aged mice up to 30 d after 5-FU treatment (Extended Data Fig. 9g–h). scRNA-seq of sorted young and aged ECs showed largely overlapping transcriptome profiles with few differentially expressed genes, mainly indicating a lack of proliferating ECs within the aged samples (Extended Data Fig. 9i–k and Supplementary Table 5). Jag2 expression did not recover in the aged sinusoidal niche after 5-FU and HSCs localised significantly farther from sinusoids, while their proximity to arterioles increased (Fig. 7f–h). Considering that we detected no change in the frequency and proliferation rate of HSCs in the aged BM after 5-FU (Fig. 7b and Extended Data Fig. 9l–m), we conclude that HSCs probably relocated to the arteriolar niche. Since young mice fully recover after 5-FU treatment (Fig. 7d) and 5-FU did not directly affect HSCs in both young and aged mice (Fig. 7e), our data strongly support that the Jag2$^+$ sinusoidal niche is critical for maintaining functional HSCs in aged animals.

Discussion

Collectively, our data imply that aLR-HSCs, when compared with anLR-HSCs, present with the highest regenerative potential; a less pronounced expansion compared with young cells; an absence of clustering; high cytosol and epigenetic polarity; canonical Wnt signaling and an overall 'younger' transcriptome profile. In addition, we showed here that aLR-HSCs are exclusively found at sinusoidal niches that are essential for maintaining haematopoiesis in aged mice. HSCs adjacent to sinusoids are proximal to a different kind of perisinusoidal cells, and our data cannot help determine whether a specific perisinusoidal cell type is required to maintain stem cell function on ageing. Still, transplantation assays, histological data and in silico modelling all convey that the sinusoidal/Nes-GFP^{low} niche is uniquely phenotypically and functionally preserved on ageing, while in general, most of the other niches and the proximity of HSCs to niche cells are significantly altered on ageing (Extended Data Fig. 10a). According to our deep learning approach, the proximity of selected niche cells to HSCs can be successfully used to predict if a given stem cell is young or old.

In light of a supportive contribution of the niche to the intrinsic function of HSCs[46], our data strongly imply that the sinusoidal/

Fig. 5 | Jag2 maintains aged LR-HSCs at sinusoids. a, Diffusion map of normalized gene expression data of old LR- and nLR-HSCs, young LR-HSCs and young HSCs (young data was reanalysed from ref. [23]). **b**, Heatmap showing the relative expression levels of differentially expressed genes. **c**, Gene ontology analysis of genes that are upregulated in aged LR-HSCs (detected using ToppGene). **d**, *Rbpj* and *Hes1* are upregulated in aged LR-HSCs. Values relate to single cells and refer to DESeq-normalized and baseline logged (FPKM). Data are plotted as average population expression ± s.d. ($n = 28$ nLR-HSCs, $n = 37$ LR-HSCs). **e**, Jag2 expression (red) at sinusoidal vessels (blue) and perisinusoidal Nes-GFP^{low} cells (green). **f**, Jag2 expression (red) at arterioles (blue, CD31/CD144) and periarteriolar Nes-GFP^{high} cells (green). **g**, Flow cytometry percentages of Nes-GFP^{high} cells, expressing Dll1 ($n = 4$ young, $n = 3$ old), Jag1 ($n = 3$ young, $n = 3$ old) and Jag2 ($n = 4$ young, $n = 3$ old). **h**, Flow cytometry percentages of Nes-GFP^{low} cells expressing Dll1 ($n = 2$ young, $n = 2$ old), Jag1 ($n = 5$ young, $n = 3$ old) and Jag2 ($n = 5$ young, $n = 3$ old). **i**, Flow cytometry percentages of endothelial cells expressing Dll1 ($n = 2$ young, $n = 2$ old), Jag1 ($n = 5$ young, $n = 3$ old) and Jag2 ($n = 5$ young, $n = 3$ old). **j**, Old mice were injected twice, 24 h apart with 15 mg kg^{-1} of either Jag2 blocking antibody or isotype control antibody. **k–n**, HSCs in distal-diaphyseal-femoral central BM from old mice treated with Jag2 blocking antibody and isotype control (CD150$^+$ in red and exclusion markers CD48$^-$, CD41$^-$, Lin$^-$ in white) (**k**); percentage of clustered HSCs (1,265 and 109 HSCs from $n = 4$ and $n = 3$ areas; 3 old mice per group) (**l**), percentage of clustered Ki-67$^+$ HSCs (966 and 109 HSCs per group from $n = 3$ areas per group; 2/3 mice per group) (**m**), and percentage of clustered HSCs adjacent to sinusoids (1,113 and 109 HSCs from $n = 4$ and $n = 3$ areas, 3 mice per group) (**n**) from the same samples. Experiments in **e**, **f** and **k** were repeated independently three times with similar results. In **g–i** and **l–n** data represent the mean ± s.e.m and statistical significance was assessed using two-tailed unpaired *t*-tests. *$P = <0.05$. Scale bars, 20 µm (**e**, **f**); 100 µm (**k**). See also Extended Data Fig. 7, 8 and Supplementary Video 6 and Source Data Fig. 5.

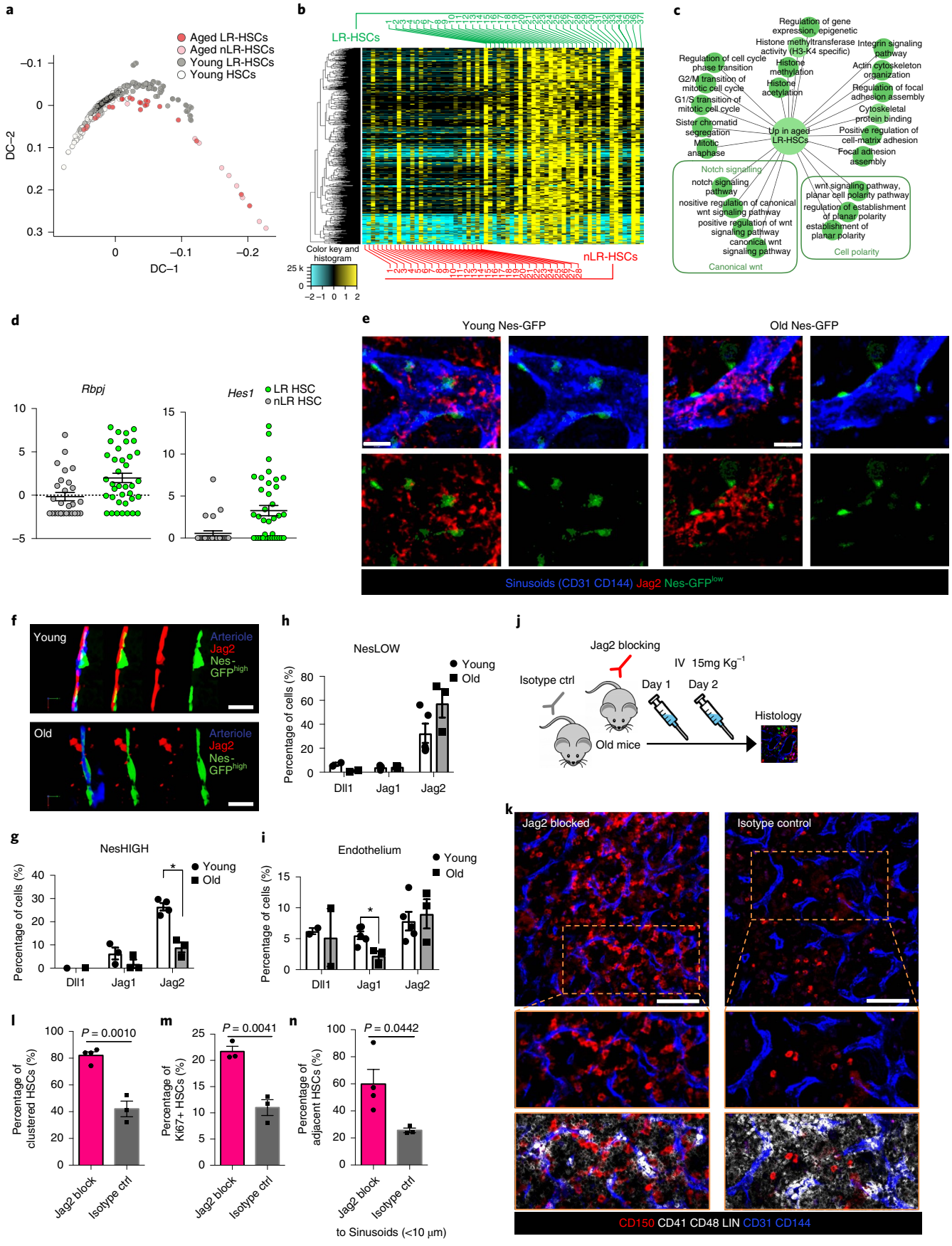
a
Aged LR-HSCs
Aged nLR-HSCs
Young LR-HSCs
Young HSCs
DC–2
DC–1
b
LR-HSCs
nLR-HSCs
Color key and histogram
c
Regulation of gene expression, epigenetic
Histone methyltransferase activity (H3-K4 specific)
Integrin signaling pathway
Regulation of cell cycle phase transition
Histone methylation
Actin cytoskeleton organization
G2/M transition of mitotic cell cycle
Histone acetylation
Regulation of focal adhesion assembly
G1/S transition of mitotic cell cycle
Cytoskeletal protein binding
Sister chromatid segregation
Up in aged LR-HSCs
Positive regulation of cell-matrix adhesion
Mitotic anaphase
Focal adhesion assembly
Notch signaling
notch signaling pathway
nositive regulation of canonical wnt signaling pathway
positive regulation of wnt signaling pathway
canonical wnt signaling pathway
Canonical wnt
wnt signaling pathway, planar cell polarity pathway
regulation of establishment of planar polarity
establishment of planar polarity
Cell polarity
d
Rbpj
Hes1
LR HSC
nLR HSC
e
Young Nes-GFP
Old Nes-GFP
Sinusoids (CD31 CD144) Jag2 Nes-GFPlow
f
Young
Old
Arteriole
Jag2
Nes-GFPhigh
g
NesHIGH
Percentage of cells (%)
Young
Old
Dll1
Jag1
Jag2
h
NesLOW
i
Endothelium
j
Jag2 blocking
IV 15mg Kg−1
Isotype ctrl
Day 1
Day 2
Histology
Old mice
k
Jag2 blocked
Isotype control
CD150 CD41 CD48 LIN CD31 CD144
l
P = 0.0010
Percentage of clustered HSCs (%)
Jag2 block
Isotype ctrl
m
P = 0.0041
Percentage of Ki67+ HSCs (%)
n
P = 0.0442
Percentage of adjacent HSCs (%)
to Sinusoids (<10 μm)

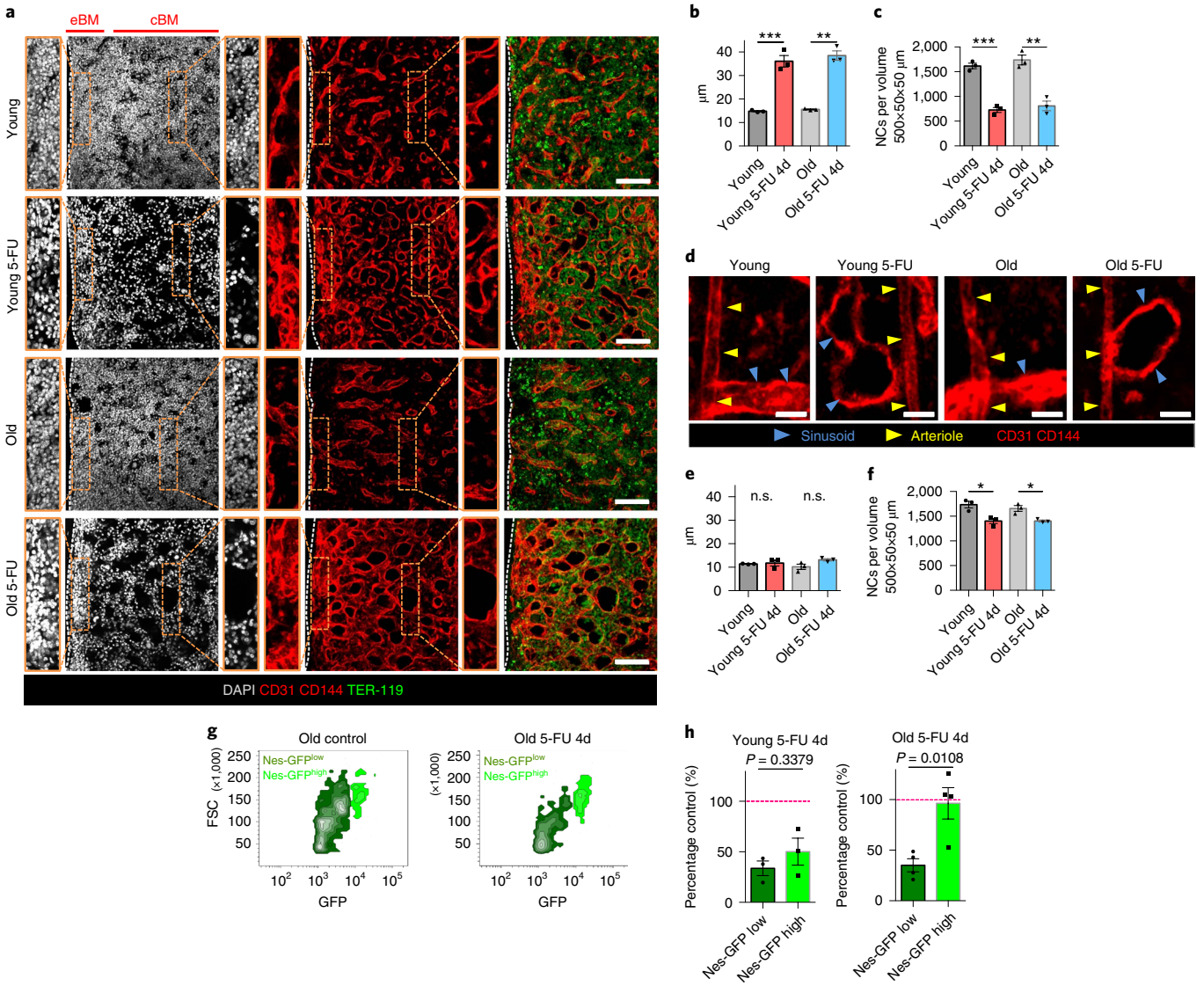

Fig. 6 | 5-FU treatment specifically disrupts sinusoidal niches. a, *Z*-stacked whole-mount images showing vasculature (red), nucleated cells (4′,6-diamidino-2-phenylindole, DAPI) and erythroid cells (green) in long bones from young and old mice 4 d after 5-FU administration, as well as untreated controls. Endosteal BM (eBM) and central BM (cBM) at <50 μm and ≥50 μm from the endosteum (dashed line), respectively, are also shown. **b**,**c**, Quantification of BV diameter (**b**) and total nucleated cell (NC) numbers per volume (**c**) in stacked images in central BM (≥50 μm from endosteal) from post-4-day-5-FUtreated and non-treated young and old mice (**b**, means of 135, 81, 151 and 85 BVs from $n = 3$ areas; **c**, $n = 3$ areas, two mice per group). **d**, Images showing arterioles (yellow arrowheads) and sinusoids (blue arrowheads) in BM from 5-FU treated and non-treated young and old mice; CD31/CD144 are shown in red. **e**,**f**, Quantification of BV diameter (**e**) and total nucleated cell (NC) numbers per volume (**f**) in *z*-stacked images in endosteal BM (<50 μm from endosteal) from post-4-day-5-FU-treated (4d) and non-treated young and old mice (**e**, means of 46, 35, 48 and 36 BVs from $n = 3$ areas; **f**, $n = 3$ areas, two mice per group). **g**, Representative flow density plot of old control and 5-FU treated Nes-GFP cells. **h**, Percentage of absolute number of Nes-GFP^{low} and Nes-GFP^{high} cells in BM of 5-FU-treated young ($n = 3$ mice) and old mice ($n = 4$ mice) to control. The experiments in **a**, **d** and **g** were repeated independently three times with similar results. Data represent the mean ± s.e.m. In **b**, **c**, **e**, **f** and **h** the statistical significance was assessed using two-tailed unpaired *t*-tests. $^{*}P = <0.05$, $^{**}P = <0.01$, $^{***}P = <0.001$, n.s., not significant; scale bars, 100 μm (**a**); 20 μm (**d**). See also Extended Data Fig. 9 and Source Data Fig. 6.

Nes-GFP^{low} niche in aged mice, via Jag2 signalling, preserves a more pristine function of HSCs located close to it. The deficiency in endothelial Jag2 recovery after 5-FU treatment (Fig. 7f,g) may be a critical aspect defeating haematopoietic stem cell functional preservation in old mice. These data are surprising when considering previous findings that ruled out a significant effect of cell-autonomous canonical Notch signaling on HSC maintenance in vivo[47]. However, haematopoietic stress, as observed after 5-FU treatment and ageing, was not directly investigated. Our data are consistent indeed with a more recent report highlighting specifically the importance of endothelial Jag2 after myelosuppression[48]. Collectively, these findings add to our understanding of how a specific BM niche can impact HSC fate in the elderly in general, and particularly in the context of specific chemotherapeutic interventions.

Online content

Any methods, additional references, Nature Research reporting summaries, source data, extended data, supplementary information, acknowledgements, peer review information, details of author contributions and competing interests, and statements of

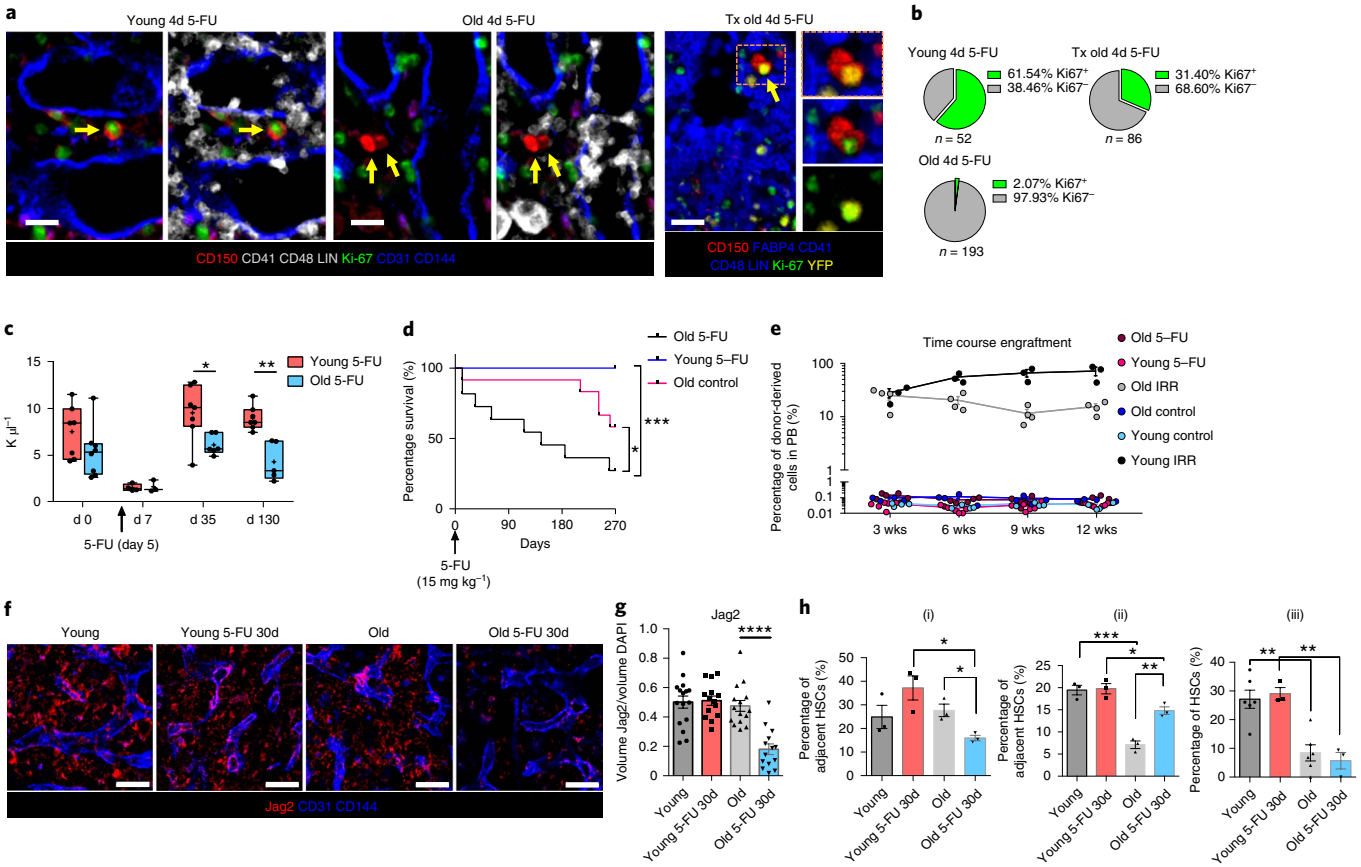

Fig. 7 | 5-FU treatment impairs haematopoiesis and survival of old mice. a, Young, old and old YFP$^+$ transplanted (Tx old) HSCs in BM 4 d after 5-FU treatment. Arrows indicate HSCs and Ki-67 HSCs are shown in green. **b**, Percentages of Ki-67$^+$ and Ki-67$^-$ HSCs detected in young, old and Tx old mice 4 d after 5-FU treatment. **c**,**d**, White blood cell (WBC, given in K µl^{-1}) count (**c**) and survival (**d**) after 5-FU administration for young and old mice; survival of old control mice is also shown. Old 5-FU treated mice median survival was 145 days (**c**, 5-FU young, $n=7$ mice; 5-FU old, $n=8$ mice ; **d**, 5-FU young, $n=12$ mice; 5-FU old, $n=11$; old control, $n=12$). **e**, Kinetics of engrafted cells in 5-FU preconditioned, lethally irradiated (11 Gy) and unconditioned control young and old transplanted mice (young 5-FU, aged 5-FU $n=6$; aged IRR, aged control, young control, $n=4$; young IRR $n=3$). **f**, Vasculature (blue) and Jag2 (red) in young and old mice 30 d post5-FU treatment. **g**, Ratio of Jag2 signal to DAPI in *z*-stacked images of BM from non-treated young ($n=16$ areas from two mice), non-treated old ($n=15$ areas from two mice), 30 d post-5-FU-treated young ($n=15$ areas from 3 mice) and 30 d post-5-FU-treated old mice ($n=14$ areas from two mice). **h**, Percentage of HSCs in proximity to sinusoids (i), arterioles (ii) and in the endosteal area (iii) (for non-treated young and old, $n=3$ (to sinusoids), $n=3$ (to arterioles), and $n=6$ mice (to endosteum) per group; for 30 d post-5-FU-treated young and old, $n=3$ (to sinusoids), $n=3$ (to arterioles) and $n=3$ mice (to endosteum) per group). Experiments in **a** and **f** were repeated independently three times with similar results. In **g** and **h**, the data represent the mean ± s.e.m. In **g** and **h**, the statistical significance was assessed by two-tailed unpaired *t*-tests (**g**,**h**), by a two-way ANOVA test (**c**) and by a one-sided log-rank (Mantel-Cox) test (**d**). *P= <0.05, **P = <0.01, ***P = <0.001, ****P = <0.0001. Scale bars, 20 µm (**a**); 50 µm (**f**). Statistical details for **c** and **e** are available in Source Data Fig. 7. See also Extended Data Fig. 9 and Supplementary Table 5.

code and data availability are available at https://doi.org/10.1038/s41556-019-0418-y.

Received: 11 March 2019; Accepted: 30 September 2019;
Published online: 4 November 2019

References

1. Kunisaki, Y. et al. Arteriolar niches maintain haematopoietic stem cell quiescence. *Nature* **502**, 637–643 (2013).
2. Ding, L., Saunders, T. L., Enikolopov, G. & Morrison, S. J. Endothelial and perivascular cells maintain haematopoietic stem cells. *Nature* **481**, 457–462 (2012).
3. Acar, M. et al. Deep imaging of bone marrow shows non-dividing stem cells are mainly perisinusoidal. *Nature* **526**, 126–130 (2015).
4. Itkin, T. et al. Distinct bone marrow blood vessels differentially regulate haematopoiesis. *Nature* **532**, 323–328 (2016).
5. Chen, J. Y. et al. Hoxb5 marks long-term haematopoietic stem cells and reveals a homogenous perivascular niche. *Nature* **530**, 223–227 (2016).
6. Calvi, L. M. et al. Osteoblastic cells regulate the haematopoietic stem cell niche. *Nature* **425**, 841–846 (2003).
7. Guidi, N. et al. Osteopontin attenuates aging-associated phenotypes of hematopoietic stem cells. *EMBO J.* **36**, 840–853 (2017).
8. Heazlewood, S. Y. et al. Megakaryocytes co-localise with hemopoietic stem cells and release cytokines that up-regulate stem cell proliferation. *Stem Cell Res.* **11**, 782–792 (2013).
9. Zhao, M. et al. Megakaryocytes maintain homeostatic quiescence and promote post-injury regeneration of hematopoietic stem cells. *Nat. Med.* **20**, 1321–1326 (2014).
10. Bruns, I. et al. Megakaryocytes regulate hematopoietic stem cell quiescence through CXCL4 secretion. *Nat. Med.* **20**, 1315–1320 (2014).
11. Mendez-Ferrer, S. et al. Mesenchymal and haematopoietic stem cells form a unique bone marrow niche. *Nature* **466**, 829–834 (2010).
12. Haylock, D. N. et al. Hemopoietic stem cells with higher hemopoietic potential reside at the bone marrow endosteum. *Stem Cells* **25**, 1062–1069 (2007).
13. Akunuru, S. & Geiger, H. Aging, Clonality, and Rejuvenation of Hematopoietic Stem Cells. *Trends Mol. Med.* **22**, 701–712 (2016).
14. Geiger, H., de Haan, G. & Florian, M. C. The ageing haematopoietic stem cell compartment. *Nat. Rev. Immunol.* **13**, 376–389 (2013).

15. Morrison, S. J., Wandycz, A. M., Akashi, K., Globerson, A. & Weissman, I. L. The aging of hematopoietic stem cells. *Nat. Med.* **2**, 1011–1016 (1996).
16. Rossi, D. J. et al. Cell intrinsic alterations underlie hematopoietic stem cell aging. *Proc. Natl Acad. Sci. USA* **102**, 9194–9199 (2005).
17. Kamminga, L. M. et al. Impaired hematopoietic stem cell functioning after serial transplantation and during normal aging. *Stem Cells* **23**, 82–92 (2005).
18. Beerman, I., Maloney, W. J., Weissmann, I. L. & Rossi, D. J. Stem cells and the aging hematopoietic system. *Curr. Opin. Immunol.* **22**, 500–506 (2010).
19. Maryanovich, M. et al. Adrenergic nerve degeneration in bone marrow drives aging of the hematopoietic stem cell niche. *Nat. Med.* **24**, 782–791 (2018).
20. Bockamp, E. et al. Tetracycline-controlled transgenic targeting from the SCL locus directs conditional expression to erythrocytes, megakaryocytes, granulocytes, and c-kit-expressing lineage-negative hematopoietic cells. *Blood* **108**, 1533–1541 (2006).
21. Wilson, A. et al. Hematopoietic stem cells reversibly switch from dormancy to self-renewal during homeostasis and repair. *Cell* **135**, 1118–1129 (2008).
22. Walter, D. et al. Exit from dormancy provokes DNA-damage-induced attrition in haematopoietic stem cells. *Nature* **520**, 549–552 (2015).
23. Cabezas-Wallscheid, N. et al. Vitamin a-retinoic acid signaling regulates hematopoietic stem cell dormancy. *Cell* **169**, 807–823 (2017).
24. Essers, M. A. et al. IFNalpha activates dormant haematopoietic stem cells in vivo. *Nature* **458**, 904–908 (2009).
25. Bernitz, J. M., Kim, H. S., MacArthur, B., Sieburg, H. & Moore, K. Hematopoietic stem cells count and remember self-renewal divisions. *Cell* **167**, 1296–1309 (2016).
26. Waskow, C. et al. Hematopoietic stem cell transplantation without irradiation. *Nat. Methods* **6**, 267–269 (2009).
27. Florian, M. C. et al. A canonical to non-canonical Wnt signalling switch in haematopoietic stem-cell ageing. *Nature* **503**, 392–396 (2013).
28. Florian, M. C. et al. Cdc42 activity regulates hematopoietic stem cell aging and rejuvenation. *Cell Stem Cell* **10**, 520–530 (2012).
29. Grigoryan, A. et al. LaminA/C regulates epigenetic and chromatin architecture changes upon aging of hematopoietic stem cells. *Genome Biol.* **19**, 189 (2018).
30. Florian, M. C. et al. Aging alters the epigenetic asymmetry of HSC division. *PLoS Biol.* **16**, e2003389 (2018).
31. Maryanovich, M., Takeishi, S. & Frenette, P. S. Neural regulation of bone and bone marrow. *Cold Spring Harb. Perspect. Med.* **4**, a031344 (2018).
32. Kusumbe, A. P. et al. Age-dependent modulation of vascular niches for haematopoietic stem cells. *Nature* **532**, 380–384 (2016).
33. Spencer, J. A. et al. Direct measurement of local oxygen concentration in the bone marrow of live animals. *Nature* **508**, 269–273 (2014).
34. Zhang, Y. et al. CXCR4/CXCL12 axis counteracts hematopoietic stem cell exhaustion through selective protection against oxidative stress. *Sci. Rep.* **6**, 37827 (2016).
35. Sugiyama, T., Kohara, H., Noda, M. & Nagasawa, T. Maintenance of the hematopoietic stem cell pool by CXCL12-CXCR4 chemokine signaling in bone marrow stromal cell niches. *Immunity* **25**, 977–988 (2006).
36. Broxmeyer, H. E. et al. DEK regulates hematopoietic stem engraftment and progenitor cell proliferation. *Stem Cells Dev.* **21**, 1449–1454 (2012).
37. Solaimani Kartalaei, P. et al. Whole-transcriptome analysis of endothelial to hematopoietic stem cell transition reveals a requirement for Gpr56 in HSC generation. *J. Exp. Med.* **212**, 93–106 (2015).
38. Holmfeldt, P. et al. Functional screen identifies regulators of murine hematopoietic stem cell repopulation. *J. Exp. Med.* **213**, 433–449 (2016).
39. Borggrefe, T. & Oswald, F. The Notch signaling pathway: transcriptional regulation at Notch target genes. *Cell. Mol. Life Sci.* **66**, 1631–1646 (2009).
40. Kojika, S. & Griffin, J. D. Notch receptors and hematopoiesis. *Exp. Hematol.* **29**, 1041–1052 (2001).
41. Guiu, J. et al. Hes repressors are essential regulators of hematopoietic stem cell development downstream of Notch signaling. *J. Exp. Med.* **210**, 71–84 (2013).
42. Shimizu, K. et al. Binding of Delta1, Jagged1, and Jagged2 to Notch2 rapidly induces cleavage, nuclear translocation, and hyperphosphorylation of Notch2. *Mol. Cell. Biol.* **20**, 6913–6922 (2000).
43. Kopp, H. G., Hooper, A. T., Avecilla, S. T. & Rafii, S. Functional heterogeneity of the bone marrow vascular niche. *Ann. N. Y. Acad. Sci.* **1176**, 47–54 (2009).
44. Kopp, H. G. et al. Tie2 activation contributes to hemangiogenic regeneration after myelosuppression. *Blood* **106**, 505–513 (2005).
45. Zhou, B. O. et al. Bone marrow adipocytes promote the regeneration of stem cells and haematopoiesis by secreting SCF. *Nat. Cell Biol.* **19**, 891–903 (2017).
46. Baryawno, N., Severe, N. & Scadden, D. T. Hematopoiesis: reconciling historic controversies about the niche. *Cell Stem Cell* **20**, 590–592 (2017).
47. Maillard, I. et al. Canonical notch signaling is dispensable for the maintenance of adult hematopoietic stem cells. *Cell Stem Cell* **2**, 356–366 (2008).
48. Guo, P. et al. Endothelial jagged-2 sustains hematopoietic stem and progenitor reconstitution after myelosuppression. *J. Clin. Invest.* **127**, 4242–4256 (2017).

Methods

Mice. SCL-tTAxH2B-GFP double heterozygous mouse bones were obtained from the Milsom's laboratory (Deutsches Krebsforschungszentrum, Division of Experimental Hematology,). Technical details of the mouse Dox treatments were previously described[22]. The Nes-GFP transgenic mouse line was obtained from the Méndez-Ferrer's laboratory (Wellcome Trust-Medical Research Council Cambridge Stem Cell Institute and Department of Hematology, University of Cambridge). C57BL/6 mice (8–16 weeks old) were obtained from Janvier. Aged C57BL/6 mice (20–26 months old) were obtained from the internal divisional stock (derived from mice obtained from both The Jackson Laboratory and Janvier), as well as from NIA/Charles River. *Rag2*$^{-/-}\gamma c^{-/-}$*Kit*$^{W/Wv}$ mice were obtained from the internal divisional stock (derived from mice obtained from Hans-Reimer Rodewald (Deutsches Krebsforschungszentrum, Division of Cellular Immunology, Heidelberg)[26]). *Rag2*$^{-/-}\gamma c^{-/-}$*Kit*$^{W/Wv}$ recipient mice are devoid of B and T cells per definition[26,49]. Young and aged AcRFP and AcYFP mice were obtained from the internal divisional stock (derived from mice obtained from H. J. Fehling, Institute of Immunology, Ulm University). Briefly, Pan-YFP mice carrying constitutively active ROSA26-tdYFP alleles (indicated in the manuscript as AcYFP mice) were obtained from H. J. Fehling (Institute of Immunology, Ulm University), and were previously generated by intercrossing C57BL/6-Gt(ROSA)26Sortm1Hjf/Ieg mice[50] with animals from a germline Cre-deleter strain[51]. Offspring in which the ROSA26-driven fluorescent tdYFP reporter had been activated irreversibly as the result of loxP/Cre-mediated recombination in the germline were backcrossed for >10 generations onto C57BL/6, thereby eliminating the Cre recombinase transgene. AcYFP mice were used as homozygotes. Young AcCFP mice were obtained from the internal divisional stock (derived from mice obtained from Y. Zheng, Cincinnati Children Hospital Medical Centre). All mice were housed in the animal barrier facility under pathogen-free conditions at the University of Ulm. Throughout the manuscript, young mice are between 10 and 16 weeks old and aged mice are at least 80 weeks old. To induce myeloablation by 5-FU, mice were intraperitoneally administered one dose of 5-FU (150 mg kg^{-1}). Young mice were treated with 5-FU at 10 weeks of age; old mice were treated with 5-FU at 76 weeks of age. Mice for this study were randomly selected and survival was followed up to 270 d after 5-FU administration. To assess the statistical significance of differences in survival, we performed log rank Mantel Cox test. All statistical tests were performed using GraphPad with Prism (version 7.0), following its Statistics Guide. Animals were not selected on the basis of gender.

Ethical compliance for mouse experiments. All mouse experiments were performed in compliance with the ethical regulations according to the German Law for Welfare of Laboratory Animals and were approved by the Institutional Review Board of the Ulm University, as well as by the state government of Baden-Württemberg, Regierungspraesidium Tuebingen.

Flow cytometry and cell sorting. Peripheral blood (PB) and BM cell immunostaining was performed according to standard procedures and samples were analysed on a LSRII flow cytometer (BD Biosciences). Monoclonal antibodies to Ly5.2 (clone 104, eBioscience) and Ly5.1 (clone A20, eBioscience) were used to distinguish recipient from donor cells. For PB and BM lineage analysis, the antibodies used were all from eBioscience: anti-CD3ε (clone 145-2C11), anti-B220 (clone RA3-6B2), anti-Mac-1 (clone M1/70) and anti-Gr-1 (clone RC57BL/6-8C5). Lineage FACS analysis data are plotted as the percentage of B220$^+$, CD3$^+$ and Myeloid (Gr-1$^+$, Mac-1$^+$ and Gr-1$^+$ Mac-1$^+$) cells among donor-derived cells in case of a transplantation experiment or among total white blood cells. Information on the gating strategy used can be found in Extended Data Fig. 10e. As for early haematopoiesis analysis, mononuclear cells were isolated by low-density centrifugation (Histopaque 1083, Sigma) and stained with a cocktail of biotinylated lineage antibodies. Biotinylated antibodies used for lineage staining were all rat anti-mouse antibodies: anti-CD11b (clone M1/70), anti-B220 (clone RA3-6B2), anti-CD5 (clone 53–7.3) anti-Gr-1 (clone RB6-8C5), anti-Ter119 and anti-CD8a (clone 53–6.7) (eBioscience). After lineage depletion by magnetic separation (Dynalbeads, Invitrogen), cells were stained with anti-Sca-1 (clone D7) (eBioscience), anti-c-kit (clone 2B8) (eBioscience), anti-CD34 (clone RAM34) (eBioscience), anti-CD127 (clone A7R34) (eBioscience), anti-Flk-2 (clone A2F10) (eBioscience), anti CD48 (clone HM48-1, BioLegend), anti-CD150 (clone TC15-12F12.2, BioLegend) and Streptavidin (eBioscience). Early haematopoiesis FACS analysis data were plotted as the percentage of long-term haematopoietic stem cells (HSCs, gated as LSK CD34$^{-/low}$ Flk2$^-$CD48$^-$ CD150$^+$), short-term haematopoietic stem cells (ST-HSCs, gated as LSK CD34$^+$ Flk2-) and lymphoid-primed multipotent progenitors (LMPPs, gated as LSK CD34$^+$ Flk2$^+$)[43] distribution among donor-derived LSKs (Lin- c-kit$^+$ Sca-1$^+$ cells). To isolate HSCs, lineage depletion was performed to enrich for lineage negative cells. Lineage negative cells were then stained as mentioned before and sorted using a BD FACS Aria III (BD Bioscience).

To investigating Notch ligand expression on BM stromal cells, endothelial cells and Nes-GFP$^+$ cells were gated according to Extended Data Fig. 10b,d. Additional antibody staining was performed with anti-Jag1 APC (clone HMJ1-29, BioLegend), anti-Jag2 eFluor660 (clone HMJ2-1, Invitrogen), anti-Dll1 APC (HMD1-3, BioLegend) and the percentage of positive cells was gated against isotype control (APC Armenian Hamster IgG, BioLegend; eFluor660 Armenian Hamster IgG, ebioscience) stained matching samples. Detailed information about all antibodies used in this study and their validation is provided in Supplementary Table 6.

Whole-mount immunofluorescence staining. After optional intravenous. injection of APC-anti-CD31 (clone MEC13.3, BioLegend) and Alexa Fluor 647-anti-CD144 (clone BV13, BioLegend) antibodies, bones were harvested after post-mortem heart perfusion with 4% paraformaldehyde (PFA) in phosphate-buffered saline (PBS) and were post-fixed in 4% PFA/PBS-solution for 24 h at 4 °C. Subsequently, bones were embedded without bisecting in an optimum cutting temperature compound (Tissue-Tek) and were snap frozen in liquid nitrogen and stored at −80 °C. Bones were shaved along the longitudinal axis on a cryostat until the BM cavity was exposed. The bones were purified from melting the optimum cutting temperature compound. Specimens were fixed again in 4% PFA/PBS at room temperature for 30 min. Tissues were blocked and permeabilized with buffer containing 20% donkey serum and 0.5% Triton X-100, incubated with a fluorescently labelled antibody PE-anti-CD150 or Alexa Fluor 488-anti-CD150 (both clone TC15-12F12.2, BioLegend) and Biotin-labelled primary antibodies anti-CD41 (clone MWReg30), anti-CD48 (clone HM48-1), anti-CD11b (clone M1/70), anti-B220 (clone RA3-6B2), anti-CD5 (clone 53–7.3) anti-Gr-1 (clone RB6-8C5), anti-Ter-119 and anti-CD8a (Clone 53–6.7) (eBioscience) for 1–3 days at 4 °C and stained with Streptavidin-eFluor 450 (eBioscience), Streptavidin-FITC (eBioscience) or Streptavidin-APC (eBioscience) for 2 h at room temperature. For BM staining, shaved bones were incubated with FITC-anti-Ki-67 (clone SolA15, ebioscience), armenian-hamster-PE-anti-mouse DLL4 (clone HMD4-1, BioLegend), armenian-hamster-PE-anti-mouse DLL1 (clone HMD1-5, ebioscience) or primary antibodies goat-anti-FABP4 (R&D Systems), biotinylated anti-CD41 (clone MWReg30, ebioscience), rabbit-anti-Jag2 (clone EPR3646, Abcam) or rabbit-anti-Jag1 (polyclonal, Abcam) for 1–2 days at 4 °C, and stained with secondary antibodies Streptavidin-eFluor 450 (eBioscience) or fluorescently labelled donkey-anti-goat, donkey-anti-rabbit and donkey anti-armenian hamster antibodies (Jackson ImmunoResearch) for 2 h at room temperature. If necessary, the nuclei were counterstained with 4′,6-diamidino-2-phenylindole. The fluorescently labelled bone tissues were placed cut-face-down onto a 4-well microslide and were covered in antifade or PBS to prevent tissue desiccation. The preparations were examined under Zeiss LSM 710 or Leica TCS SP8 confocal microscopes and analysed with the image analysis software Volocity (v6.2, Perkin Elmer). The nearest distances from HSCs to multiple niche cell types were measured. The term arteriole includes arterial and arteriolar cell. Two-photon imaging was performed on cryo-shaved long bones using an upright Zeiss 7MP microscope. Two-photon excitation at 800 nm was achieved with a Mai Tai DeepSee Ti:Sa laser (Spectra-Physics) and fluorescence was detected using the BP 500–550 filter to detect green signal (GFP). For second-harmonic-generation microscopy, a BP485 filter was used to detect the blue signal. To visualize the microvasculature, we injected in vivo labelled PECAM-1 (CD31) and VE-Cadherin (CD144) antibodies or used FABP4 in situ[9]. LepR$^+$ cells were stained with anti-mouse Leptin R antibody (R&D Systems AF497). As for the proximity of HSCs to LepR$^+$ cells, we took into consideration only the distance between HSCs and the nearest perivascular LepR$^+$. When it was not possible to match the nearest LepR$^+$ process to an associated perivascular LepR$^+$ cell, we took the nearest perivascular LepR$^+$ cell body. For the Jag2 in vivo blocking histological analysis, the images with the highest HSC numbers in the distal-diaphyseal-femoral central BM were taken into consideration. Detailed information about all antibodies used in this study and their validation is provided in Supplementary Table 6.

Immunofluorescence staining. Freshly sorted HSCs were seeded on fibronectin-coated glass coverslips. After culturing cells were fixed with BD Cytofix Fixation Buffer (BD Biosciences) and then washed with PBS, permeabilized with 0.2% Triton X-100 (Sigma) in PBS for 20 min, and blocked with 10% Donkey Serum (Sigma) for 30 min. Primary and secondary antibody incubations were performed for 1 h at room temperature. Coverslips were mounted with ProLong Gold Antifade Reagent with or without 4′,6-diamidino-2-phenylindole (Invitrogen, Molecular Probes). The secondary antibodies for immunoflorescence staining were the anti-rat DyLight488-conjugated antibody, the anti-rat DyLight647-conjugated antibody and the anti-rabbit DyLight549-conjugated antibody (Jackson ImmunoResearch). Samples were imaged with an AxioObserver Z1 microscope (Zeiss) equipped with a 63X PH objective. Images were analysed with Zen software. Alternatively, samples were analysed with an LSM710 confocal microscope (Zeiss) equipped with a 63X objective. Primary raw data were imported into the Volocity Software package (Version 6.2, Perkin Elmer) for further processing and conversion into three-dimensional images. On average, a total of 20 dividing HSCs were singularly analysed per sample. The primary antibodies were anti-alpha tubulin antibody (Abcam, rat monoclonal ab6160) anti-Cdc42 and anti-H4K16ac obtained from Millipore and Abcam (we tested two different antibodies for each target; results were consistent. All four antibodies were rabbit polyclonal; anti-Cdc42 from Millipore was previously validated[27,28]). Detailed information about all antibodies used in this study and their validation is provided in Supplementary Table 6.

Endosteal and central BM cell population isolation. To isolate central BM cells and endosteal BM cells close to the endosteum, femora and tibiae were taken

from young and aged mice. The bones were cleaned and the associated muscle tissues removed. After the bone marrow was flushed out and lysed using RBC buffer (BioLegend), the central BM cells were obtained. The flushed bones were mortared and incubated in 1.5 mg ml^{-1} collagenase IV/PBS (Worthington) for 1.5 h at 37 °C. This endosteal BM cell fraction was filtered through a 70-µm cell strainer and counted. Central and endosteal BM cell fractions were stained with CD45.2 Monoclonal Antibody (104) PerCP-Cyanine5.5 conjugated (eBioscience), CD31-APC (BioLegend) and CD41-biotinylated + SA-FITC (eBioscience). Informating on the gating strategy is available inthe Extended Data Fig. 10b-d.

BM endothelial cell culture and HSC endothelial cell co-culture. BM endothelial were prepared from young BL6.SJL mice according to methods derived from ref. [52]. Briefly, after red blood cell lysis, BM cells were seeded on Fibronectin-coated (Takara, 1 µg µl^{-1}) 24-well plates in endothelial Medium: DMEM-HAM's F-12 (Sigma, D6421), 20% FBS, 1% P/S, 20 mM HEPES, 10 µg ml^{-1} Heparin, 50 µg ml^{-1} Endothelial Mitogen (Alfa Aeser #J65416), 5 µM SB431542 (R&D, #1614) and cultured at 37 °C, 5% CO_2, 3% O_2, with medium change every other day. After 6 days of culture, 75–90% of the cells were CD31$^+$ endothelial cells according to FACSanalysis and cell morphology. For co-culture experiments, 2,000–3,000 sorted YFP and HSCs (prepared as discussed before from AcYFP mice) were seeded on top of 6-day cultured BM endothelial cells, and the endothelial medium was supplemented with SCF, G-CSF, TPO 100 ng ml^{-1} each along with 10 µg ml^{-1} Jag2 blocking antibody (Bio X Cell BE0125[53]) or Isotype control antibody (eBioscience 14–4888–85). HSCs cultured without endothelial cells in the same medium with Jag2 blocking antibody or isotype served as control. After 44–46 h of co-culture, cells were harvested and the number of HSCs was assessed by FACS.

Preparation of binary vector maps. The in silico simulation was performed based on binary structure maps generated from processed histological data. For this, we prepared whole-mount, long bone marrow sections of young and aged Bl6 mice. We stained for different niche cell populations using immunofluorescent labelling (see the Whole-mount immunofluorescence staining section) and recorded confocal images. The *z*-stack images (z-level depth of 50 µm) were converted to two-dimensional extended-focus representations using the imaging software Volocity. Based on structure-specific immunofluorescent signals and morphologies, the images were then cleaned from secondary structures and cells, resulting in binary vector maps containing only the respective niche structure and a structure-free domain (see Supplementary Fig. 1). For each niche structure, at least three young and three aged maps were analysed, each covering an area of at least 330 µm × 770 µm with a resolution of at least 3 pixels µm^{-1}. The maps were obtained from two animals per niche structure and age group. A detailed site-to-step example of how binary structure maps where used for the simulation process is depicted in Fig. 4a: Confocal *z*-stack images of young and aged femoral bone marrow showing the niche structure of interested (here Nes-GFP^{high} cells); the relevant structure (here NesGFP^{high} cells) is selected; Signal thresholding (automatically calculated based on signal SD) and size selection filters were used to identify cellular objects and prepare binary structure maps. Blocked regions (for example by endosteum; black) were subtracted from the empty domain (white). The euclidean distance *d* of 10,000 randomly positioned entities (HSCs) within the empty domain was calculated from the edges of the niche cells (red); The distance transformation visualizes distances in all potential positions; The recorded distances of at least three different young and three different aged maps were added up and sampled again for 10,000 positions to obtain a representative probability density distribution (scale bar, 200 µm).

In silico simulation. We generated distance distributions, representing the expected distance of HSCs towards the endosteum, NesGFP^{high} cells, NesGFP^{low} cells and MKs in the young and aged setting, under the presumption of random localisation and choice of position. For each map we randomly selected 10,000 positions in the structure-free domain and recorded the Euclidean distance towards the borders of the respective niche structure. To eliminate boundary artifacts, sampled positions within 25 µm of the map edges were removed and resampled. One representative random distribution was drawn per niche structure and age group by resampling the random distributions calculated for each map of said structure and group for a total of 10,000 data points. Those representative random distributions were then used to assess the randomness of localisation of HSCs by comparing the observed in situ distances to the expected random in silico distances. In a second step, we compared the changes in random distance between young and aged within the in silicosystem. In this way, we were able to assess the systematic effect of structural changes of each isolated niche component that occurs with ageing, and predict changes in distance toward HSCs. The statistical significance of the null hypothesis that both compared distributions are derived from the same statistical population was analysed using two-sample Kolmogorov–Smirnov test. The significance levels were set to 0.05 for the comparison of observed versus observed, 1×10^{-3} for observed versus expected and 1×10^{-8} for expected versus expected. The effect size *D* indicates the supremum absolute (vertical) distance between the compared CDFs and is provided for each comparison.

Keras/TensorFlow multilayer deep learning. We employed a keras/TensorFlow binary classification model to predict young and aged HSC distances based on seven different distance measurements within the niche. We had an initial layer of 16 units, three hidden layers (16 units) and a final output layer of 1 unit (binary output). A glorot uniform initializer was used for kernel initialization, while hyperbolic tangent activation was employed for kernel activation. A stochastic gradient descent optimizer was used for model optimization along with a binary crossentropy loss measurement. The sequential model was trained by sampling data from each parameter (61 cases of young and 88 cases of aged for each iteration composed of 50 epochs), and was trained for a total of 50 iterations. A total of 80 cases (33 young and 47 aged HSCs) were put aside as a validation set (Fig. 4e). A bootstrap analysis of the validation set (500 iterations) was later used for the parameter relevance correlation analysis (Fig. 4g). There was no significant difference between the parameters' correlation coefficients ($n = 500$ correlation coefficients based on 500 iterations; each iteration round is performed by subsampling the training set ($n = 149$ cases) and conducting a correlation/association test to help distinguish which features are relevant for age classification).

Single cell RNA preparation of LR-HSCs and nLR-HSCs. Single LR-HSCs were sorted based on GFP expression (positive and negative). Cells were cultured overnight without growth factors at 3% O_2 and washed twice with PBS before processing.

Single cells were processed using the SMART-Seq v4 Ultra Low Input RNA Kit for Sequencing (Clontech Laboratories) according to the manufacturer's instructions. Amplified cDNA was purified with Agencourt AMPure XP beads (Beckman Coulter) before library preparation with a NextEra XT DNA Library Preparation kit (Illumina) according to the manufacturer's instructions. Library DNA was purified with AMPure XP beads and quantified using Agilent Bioanalyser for manual library normalization. Pooled libraries were subjected to next generation sequencing in Hi-Seq 2500, for pair end 75 bp sequencing.

Single-cell RNA preparation from CD31$^+$ endothelial cells. Young and aged BM CD45-CD31$^+$ endothelial cells were sorted from prepared endosteal tissue into IMDM (Lonza) and 10% FCS buffer (Sigma). Cells were frozen in IMDM with 20% FCS and 10% DMSO (Sigma). Endothelial cells were then thawed, washed once in warm PBS, and subjected immediately to encapsulation in oil droplets using the chromium system (10x Genomics). cDNA synthesis and library preparation were carried out according to the manufacturer's instructions for 3′ end counting. Polymerase chain reaction cycles for both cDNA synthesis and amplification were adjusted for each sample individually to the number of cells loaded and the cDNA yield respectively. Samples were pooled and sequenced on a HiSeq3000 sequencer (Illumina). Five libraries were prepared with three biological replicates.

RNA sequencing analysis of LR-HSCs and nLR-HSCs. Following removal of barcodes and primers, raw reads were aligned to the mm10 mouse genome with annotations provided by UCSC using a proprietary Burrow–Wheeler Transform alignment (COBWeb). Aligned reads were used to compute reads per kilobase per million reads using an EM-algorithm for 38,186 transcripts. Data were normalized using the DESeq algorithm and baselined to the median of all samples. A moderated *t*-test was used to identify significantly differentially regulated genes between LR-HSCs and nLR-HSCs, with significance set at $P = < 0.05$ and FC > 3. Ontological analysis was performed in ToppGene (toppgene.cchmc.org), which gathers data from over 30 ontological repositories. Figures were generated using ToppCluster (toppcluster.cchmc.org) and Cytomap. All data processing and analyses were performed in Strand Next Generation Sequencing. Sequencing data are available under GEO accession number GSE129726.

RNA-sequencing cross-analysis of aged LR-HSCs and nLR-HSCs versus young LR-HSCs and HSCs. Raw alignment data of young LR-HSCs and HSCs reported by Cabezas-Wallscheid et al.[23] was obtained via the accession number ArrayExpress: E-MTAB-4547. Alignment and low-level processing of the data was performed in parallel with our dataset of aged LR-HSCs and nLR-HSCs according to methods outlined in ref. [23]. Cell filtering on both datasets was performed with reduced stringency (>25,000 reads and >500 detected genes per library). Diffusion map representations of log-transformed, size-factor normalized expression data were generated using the R package destiny[54]. Sequencing data are available under the gene expression omnibus accession number GSE129726.

RNA sequencing analysis of CD31$^+$ endothelial cells. Unique molecular identifier (UMI) counts were generated using the Cell Ranger pipeline (10x Genomics) with default settings and the provided mm10–1.2.0 reference dataset. The cells were filtered based on total number of UMIs (>1,000), total number of detected genes (>1,000, at least one read) and the percentage of mitochondrial reads (<10%) using the scater toolkit[55] (R package). Low-expressed genes were subsequently filtered out (at least 3 reads in 20 different samples). A set of 1,651 out of 3,384 cells passed all criteria, consisting of 1,218 young and 433 aged cells covering 2,517 genes. Highly variable genes were identified by using a log-linear fit to capture the relationship between mean and squared coefficient of variation of log-transformed, size-factor normalized data[56], resulting in 1,570 genes. DE analysis was performed on HVGs using DESeq2[57], resulting in 48 genes upregulated with ageing and 11

genes downregulated with ageing. The analysis was performed on raw counts and the likelihood ratio test with the experimental batches as covariables was used. Dispersions were estimated using a local fit and size factors were estimated using the 'poscounts' setting. Cell cycle states were scored based on a random forest trained on cell cycle marker genes using Cyclone[58] (implementation in R package scran[59]). Diffusion map representations were generated using the R package destiny[54]. Sequencing data are available under gene expression omnibus accession number GSE129726.

Stem cell transplants. For HSC transplantations in Extended Data Fig. 2a–e, aged (20 months old and 18 months old under Dox chase) SCL-tTAxH2B-GFP double heterozygous mice (Ly5.1$^+$) were used as donors, and *Rag2*$^{-/-}$*γc*$^{-/-}$*Kit*$^{W/Wv}$ mice (Ly5.2$^+$) were used as recipients. From the same donor mouse 10 LR-HSCs and 10 nLR-HSCs were sorted into separated Terasaki wells. Cells were checked under the microscope before injection into the retro-orbital vein of recipient mice. From each donor mouse, we transplanted 3–4 recipents receiving 10 LR-HSCs each and 3–4 recipeints receiving 10 nLR-HSCs. A total of 4 different donor mice were used for this assay. PB chimerism was determined by FACS analysis at week 4, 12, 16 and 20 post-transplant. The transplantation experiment was performed 3 times with an initial cohort of 12–14 recipient mice per group each transplant. After 20 weeks from the primary transplant, total BM from recipient mice was harvested and reinjected into a new cohort of *Rag2*$^{-/-}$*γc*$^{-/-}$*Kit*$^{W/Wv}$ recipient mice. PB chimerism was followed as for primary transplanted mice up to 20 weeks after secondary transplantation. Immunocompromised mice are highly stressed by repetitive bleedings and some of the mice died and were not included in the final analysis. Only mice that survived till end of secondary transplants were included in the statistical analysis.

For the single HSC transplantations in Extended Data Fig. 1f–h, aged (20 months old and 18 months old under Dox chase) SCL-tTAxH2B-GFP double heterozygous mice (Ly5.1$^+$) were used as donors and *Rag2*$^{-/-}$*γc*$^{-/-}$*Kit*$^{W/Wv}$ mice (Ly5.2$^+$) were used as recipients. Single HSCs were sorted into Terasaki wells. Cells were checked under the microscope before injection into the retro-orbital vein of recipient mice. A total of 7 recipient mice were used for this assay. PB chimerism was determined by FACS analysis at weeks 4, 8 and 12, post-transplant.

For the HSC transplantations in Fig. 4h, aged (>20 months old) acYFP and young (10 weeks old) acCFP mice were used as donors. 500 HSCs from acYFP and acCFP mice were sorted together in 96 multiwell (1,000 HSCs each well). Cells were checked under the microscope before injection into the retro-orbital vein of recipient mice. A total of 5 aged (>56 weeks old) and 9 young (6 weeks old) *Rag2*$^{-/-}$*γc*$^{-/-}$*Kit*$^{W/Wv}$ mice were used as recipients. Young and aged recipient mice were transplanted alongside with the same preparation of 500 CFP$^+$and 500 YFP$^+$HSCs. PB chimerism was determined by FACS analysis at week 6, 12 and 16, post-transplant.

For the HSC transplantations in Extended Data Fig. 9c, aged (>20 months old) acYFP mice were used as donors. 500 HSCs from acYFP mice were sorted in 96 multiwell plates. Cells were checked under the microscope before injection into the retro-orbital vein of recipient mice. A total of 5 young (6 weeks old) *Rag2*$^{-/-}$*γc*$^{-/-}$*Kit*$^{W/Wv}$ mice were used as recipients. Six weeks post-transplant, young recipient mice were injected with 5-FU (150 mg kg^{-1}) and were sacrificed 4 days after for histological analysis.

For the HSC transplantations in Extended Data Fig. 9e, aged (>20 months old) acYFP and young (10 weeks old) acYFP mice were used as donors. 500 HSCs from acYFP young and aged mice were sorted in 96 multiwell plates (500 HSCs in each well). Cells were checked under the microscope before injection into the retro-orbital vein of recipient mice. A total of 5 aged (>56 weeks old) and 9 young (6 weeks old) *Rag2*$^{-/-}$*γc*$^{-/-}$*Kit*$^{W/Wv}$ mice were used as recipients. Young (12 weeks old) and aged (80 weeks old) recipient C57Bl6 mice were transplanted after either 11 Gy irradiation, 4-day 5-FU injection or no pre-conditioning. Young HSCs were transplanted into young recipients and aged HSCs were transplanted into aged recipients. PB chimerism was determined by FACS analysis at week 3, 6, 9 and 12 post-transplant.

Statistical analysis. All data are plotted as mean ± standard error (s.e.m.). A paired Student's *t*-test was used to determine the significance of the difference between means of two groups. Either one-way ANOVA or two-way ANOVA were used to compare means among three or more independent groups. The variance was similar between groups that were statistically compared. Distance analysis data were analysed using a Mann–Whitney U test when a non-Gaussian distribution was observed (tested by Shapiro-Wilk and D'Agostino-Pearson omnibus test). A Bonferroni post-test to compare all pairs of data set was used when overall P value was <0.05. All statistical analyses were determined with Prism version 7.0. In each figure legend, the number (n) of biological repeats included in the final statistical analysis is indicated. Mice for experiments were randomly chosen from our in-house colonies or suppliers.

Reporting Summary. Further information on research design is available in the Nature Research Reporting Summary linked to this article.

Data availability

RNA-seq data that support the findings of this study have been deposited in the gene expression omnibus under accession code GSE129726. Previously published sequencing data that were re-analysed here are available under ArrayExpress E-MTAB-4547[23]. All other data supporting the findings of this study are available from the corresponding author on reasonable request.

References

49. Mazurier, F. et al. A novel immunodeficient mouse model–RAG2 x common cytokine receptor gamma chain double mutants–requiring exogenous cytokine administration for human hematopoietic stem cell engraftment. *J. Interferon Cytokine Res.* **19**, 533–541 (1999).
50. Luche, H., Weber, O., Nageswara Rao, T., Blum, C. & Fehling, H. J. Faithful activation of an extra-bright red fluorescent protein in "knock-in" Cre-reporter mice ideally suited for lineage tracing studies. *Eur. J. Immunol.* **37**, 43–53 (2007).
51. Schwenk, F., Baron, U. & Rajewsky, K. A cre-transgenic mouse strain for the ubiquitous deletion of loxP-flanked gene segments including deletion in germ cells. *Nucleic Acids Res.* **23**, 5080–5081 (1995).
52. Lis, R. et al. Conversion of adult endothelium to immunocompetent haematopoietic stem cells. *Nature* **545**, 439–445 (2017).
53. Elyaman, W. et al. Notch receptors and Smad3 signaling cooperate in the induction of interleukin-9-producing T cells. *Immunity* **36**, 623–634 (2012).
54. Angerer, P. et al. destiny: diffusion maps for large-scale single-cell data in R. *Bioinformatics* **32**, 1241–1243 (2016).
55. McCarthy, D. J., Campbell, K. R., Lun, A. T. & Wills, Q. F. Scater: pre-processing, quality control, normalization and visualization of single-cell RNA-seq data in R. *Bioinformatics* **33**, 1179–1186 (2017).
56. Brennecke, P. et al. Accounting for technical noise in single-cell RNA-seq experiments. *Nat. Methods* **10**, 1093–1095 (2013).
57. Love, M. I., Huber, W. & Anders, S. Moderated estimation of fold change and dispersion for RNA-seq data with DESeq2. *Genome Biol.* **15**, 550 (2014).
58. Scialdone, A. et al. Computational assignment of cell-cycle stage from single-cell transcriptome data. *Methods* **85**, 54–61 (2015).
59. Lun, A. T., McCarthy, D. J. & Marioni, J. C. A step-by-step workflow for low-level analysis of single-cell RNA-seq data with Bioconductor. *F1000Res* **5**, 2122 (2016).

Acknowledgements

We thank J. A. Cancelas (Cincinnati Children Hospital Medical Center) for advice and critical reading of the manuscript. We thank H. J. Fehling (Institute of Immunology, Ulm University) for donating AcRFP and AcYFP mice and Y. Zheng (Cincinnati Children's Hospital Medical Center, Cincinnati, Ohio, USA) for donating AcCFP mice. We thank the core facilities at Ulm University, A. Rück (Microscope Facility), for support with confocal and two-photon microscopy, as well as the Cell Sorting Facility and the Tierforschungszentrum (Animal Facility). Work in the laboratory of M.C.F. was supported by an Emmy Noether Grant (DFG) (grant nos. SFB1074 and FOR2674) to M.C.F. M.S. was supported by a PhD Degree Scholarship of the Avicenna-Studienwerk programme.

Author contributions

M.S. and M.C.F. performed and analysed the laboratory experiments. M.S. performed all histological experiments and microscopy analysis. J.P. conceived the computational model with assistance of W.d.B. and performed the bioinformatic analysis of scRNA-seq datasets with support from R.K. K.S. and G.M. assisted in transplantation procedures, bleeding, supported in cell sorting and flow analysis procedures. A.V. performed single cell RNA-seq sample preparation, supported in cell sorting and flow analysis procedures and performed in vitro co-culture experiments. V.S. supervised the mouse work and took care of breeding, ageing and preparation of the mice used for experiments. M.S. and M.C.F. designed and interpreted the experiments. J.-P.M. prepared scRNA-seq libraries from endothelial cells. N.C.-W. supported the scRNA sequencing. N.C.-W., A.T., M.D.M. and R.B. supported all the experiments involving SCL-tTAxH2B-GFP double heterozygous mice. M.A.M. developed the deep learning algorithm. H.G. helped interpret the experiments and write the manuscript. S.M.-F. supported with Nestin-GFP mice and assisted in interpreting experiments. M.S., J.P. and M.C.F. wrote the manuscript.

Competing interests

The authors declare no competing interests.

Additional information

Extended data is available for this paper at https://doi.org/10.1038/s41556-019-0418-y.

Supplementary information is available for this paper at https://doi.org/10.1038/s41556-019-0418-y.

Correspondence and requests for materials should be addressed to M.C.F.

Reprints and permissions information is available at www.nature.com/reprints.

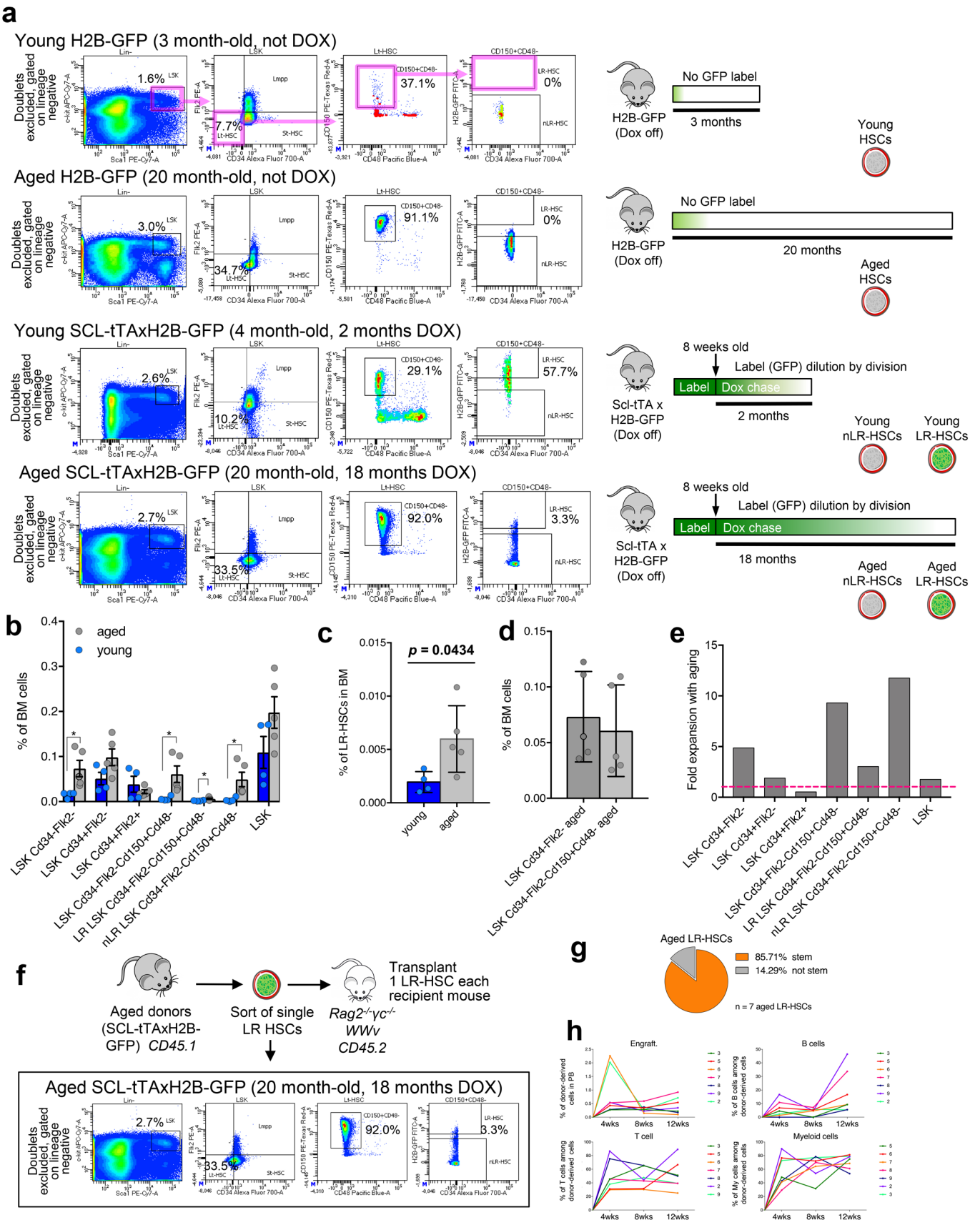

Extended Data Fig. 1 | see next page for caption.

Extended Data Fig. 1 | Aged LR-HSC pool expand less than aged nLR-HSCs and are functional long-term stem cells. a, Representative FACS dot plots of the gating strategy for LR-HSCs (Lin^-c-Kit^+ $Sca\text{-}1^+$ $Flk2^-CD34^-CD48^-CD150^+$ H2B-GFP^+) of young and aged not DOX treated H2B-GFP, and young and aged DOX treated SCL-tTAxH2B-GFP lineage-depleted BM cells and schematic representation of the experimental setups. **b**, Frequency of different HSPC subpopulations, LR-HSCs and nLR-HSCs among BM cells in young and old SCL-tTAxH2B-GFP mice after 2 and 18-months of DOX chase, respectively. **c**, Percentages of young and old LR-HSCs in BM cells in DOX treated SCL-tTAxH2B-GFP mice. **d**, Similar frequency of old LSK $CD34^-Flk2^-$HSCs and old LSK $CD34^-Flk2^-CD48^-CD150^+$ HSCs among BM cells. **e**, Fold expansion of different HSPC subpopulations, LR-HSCs and nLR-HSCs with ageing. **f**, Experimental setup of single aged LR-HSC transplantation in $Rag2^{-/-}\gamma c^{-/-}Kit^{W/Wv}$ recipient mouse and gating strategy. **g**, Pie chart showing percentage of functional long-term HSCs among single transplanted aged LR-HSCs. **h**, Blood chimerism kinetics of overall engrafted donor-derived cells and of each donor-derived lineage (B cells, T cells and myeloid cells) with single donor old LR-HSCs. The experiments in **a** were repeated four independent times with similar results. Data in **b**-**d** represent mean ± s.e.m. In **b**-**e**, $n = 4$ young and 5 aged mice. In **g**, **h** $n = 7$ recipient mice. The statistical significance was assessed by two-tailed unpaired *t*-tests. * $p < 0.05$. See also **Statistical Source Data** Extended Data Fig. 1.

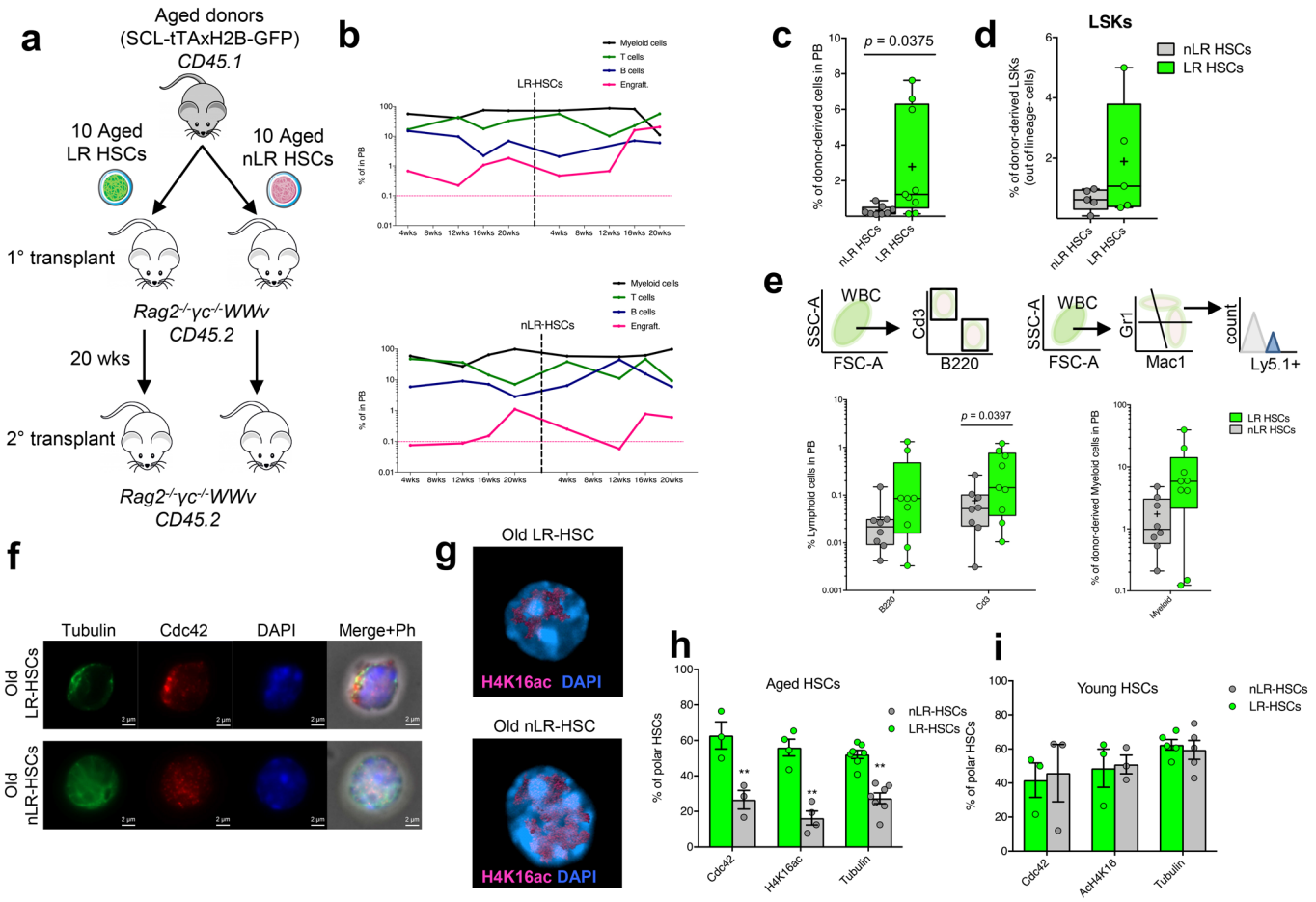

Extended Data Fig. 2 | Aged LR-HSCs show higher regenerative capacity and are polar. a, Scheme of the transplantation. **b**, Representative blood chimerism kinetics of overall engrafted donor-derived cells and of each donor-derived lineage (B cells, T cells and myeloid cells) during primary and secondary transplants of one recipient mouse transplanted with donor aLR-HSCs and one with donor anLR-HSCs. **c**, Frequency of old nLR-HSCs and old LR-HSCs donor contribution to total white blood cells (WBCs) in PB of *Rag2*$^{-/-}$*γc*$^{-/-}$*Kit*$^{W/Wv}$ recipient mice ($n = 8$ mice for nLR-HSCs, $n = 9$ mice for LR-HSCs). **d**, Frequency of aged LR- and nLR-HSCs in BM among donor-derived LSK cells in *Rag2*$^{-/-}$*γc*$^{-/-}$*Kit*$^{W/Wv}$ recipient mice. ($n = 5$ mice per group) **e**, Percentage of B cells (B220$^+$) and T cells (Cd3$^+$) in PB. *Rag2*$^{-/-}$*γc*$^{-/-}$*Kit*$^{W/Wv}$ recipient mice are devoid of B and T cells per definition[26,49] and all B220$^+$ and Cd3$^+$ cells among total WBC where donor-derived. Myeloid cells (Gr1$^+$, Mac1$^+$ and Gr1$^+$Mac1$^+$) are gated from total WBC and plotted as percentage of donor derived myeloid cells among total myeloid cells. Cartoon schemes on top of each graph depicts the gating strategy ($n = 8$ mice for nLR-HSCs, $n = 9$ mice for LR-HSCs). **f**, Representative single-cell IF images showing tubulin (green) and Cdc42 (red), in old LR-HSCs and old nLR-HSCs. Nuclei, DAPI (blue). **g**, Representative 3D reconstructed single-cell IF confocal images showing H4K16ac (magenta) in old LR-HSCs (polar) and old nLR-HSCs (apolar). Nuclei, DAPI (blue). **h**, **i**, Percentage of polar cells (**h**) in old LR-HSCs and nLR-HSCs ($n = 3$ mice for Cdc42, $n = 4$ for H4K16ac, $n = 7$ for Tubulin) and in (**i**) young LR-HSCs and nLR-HSCs ($n = 3$ mice for Cdc42, AcH4K16; $n = 5$ mice for Tubulin). Data in **h**, **i** represent mean ± s.e.m, in **c-e** data represent the 25th-75th percentiles, minimum, maximum, median (bar) and mean (cross). The statistical significance was assessed by two-tailed unpaired *t*-tests for all data beside in **e** by two-way ANOVA-test. In **e** *p* 0.0397 is related to overall lymphoid cells (B220$^+$ and Cd3$^+$ data together) between aLR-HSC and anLR-HSC samples. As for myeloid cells p = 0.09. The statistical details for **c-e** are available in **Source Data** Extended Data Fig. 2.

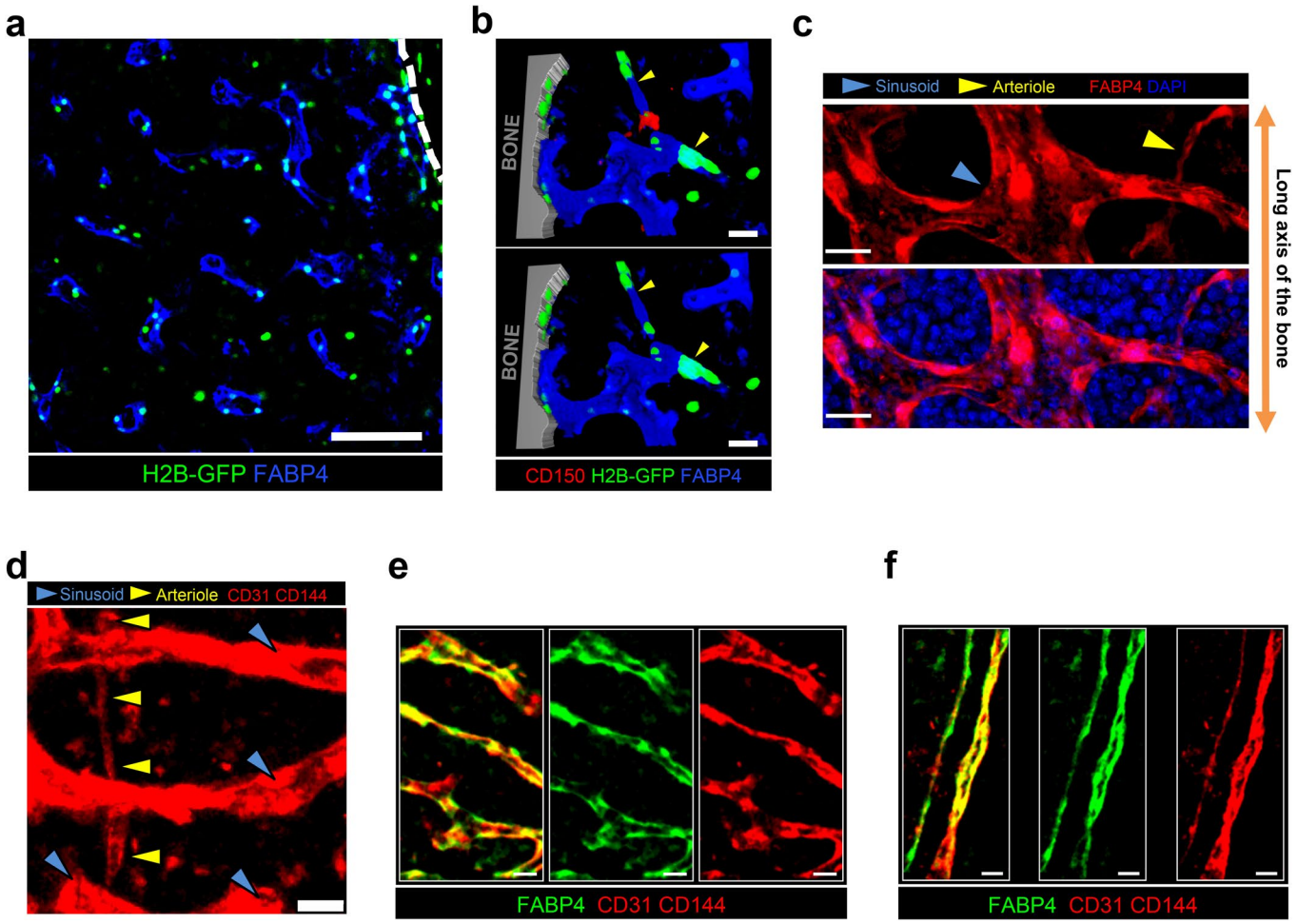

Extended Data Fig. 3 | Young LR-HSCs are located in central and endosteal BM. a, Representative stacked whole-mount images of young SCL-tTAxH2B-GFP femoral BM showing LR cells (green) and vasculature (blue). **b**, 3D reconstruction of confocal whole-mount images of young SCL-tTAxH2B-GFP femoral BM showing a CD150^{+} H2B-GFP^{+} LR cell in proximity to arterial vasculature (arrowheads) in the endosteal area. **c**, **d**, Distinction of sinusoids and arterioles in (**c**) FABP4 (red) in situ stained and (**d**) CD31/CD144 (red) i.v. stained BM: arterioles (yellow arrowheads) have small diameter with continuous staining (continuous basal lamina) and have parallel orientation to the long axis of the bone, sinusoids (blue arrowheads) present relatively larger diameter with spotted staining (fenestrated basal lamina) and are mostly transverse to the long axis. (**c**) Nuclei, DAPI (blue). **e**, **f**, Colocalization of (**e**) sinusoids and (**f**) arterioles/arteries in FABP4 (green) in situ stained and CD31/CD144 (red) i.v. stained BM. Experiments in **a-c**, **e**, **f** were repeated three independent times with similar results and in **d** at least 9 independent times with similar results. Scale bars are 100 μm (**a**); 20 μm (**b**-**f**).

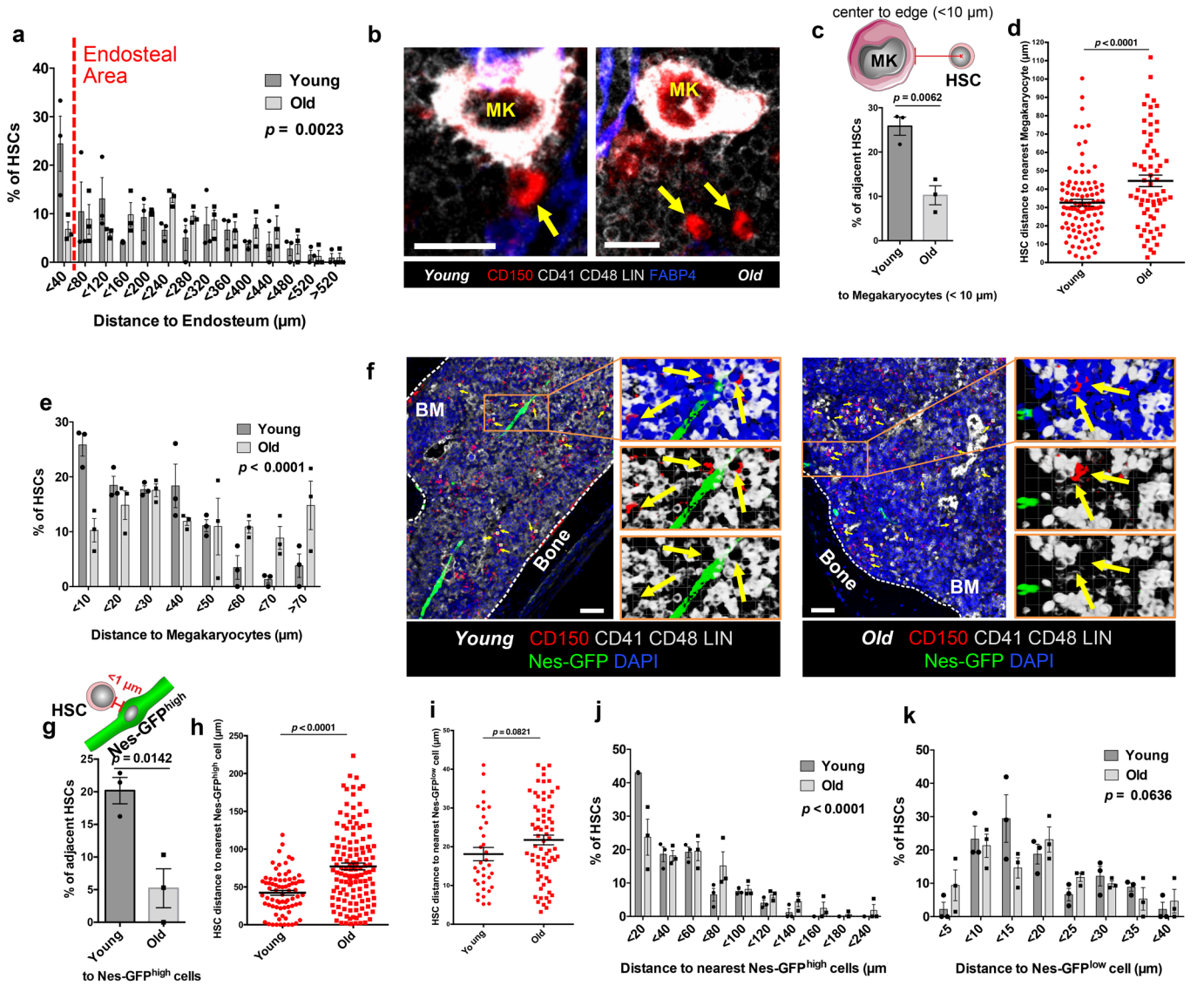

Extended Data Fig. 4 | HSC proximity to selected niche cell types is altered upon ageing. a, Distance between young and old HSCs to the nearest endosteum (192 young HSCs from 36 areas and 432 old HSCs from 17 areas, $n=3$ mice per group), **b**, Confocal images of young and old whole-mount WT femoral BM showing HSCs (arrows) and MKs. **c**, Percentage of young and old HSCs in direct proximity to MKs (<10 µm; 177 young HSCs from 34 areas and 163 old HSCs from 10 areas, $n=3$ mice per group). **d**, Mean distance of young and old HSCs to the nearest MK ($n=177$ young HSCs from 34 areas and $n=163$ old HSCs from 10 areas, 3 mice per group). **e**, Distance between young and old HSCs to the nearest MK (177 young HSCs from 34 areas and 163 old HSCs from 10 areas, $n=3$ mice per group). **f**, Confocal whole-mount images of young and old sternal Nes-GFP mice BM. Arrows (yellow) show HSCs. Nuclei, DAPI (blue). **g**, Percentage of young and old HSCs in direct contact to Nes-GFP^{high} cells (<1µm; 137 young HSCs from 9 areas and 275 old HSCs from 12, $n=3$ mice per group. **h**, Mean distance of young and old HSCs to the nearest Nes-GFP^{high} cell ($n=137$ young HSCs from 9 areas and $n=275$ old HSCs from 12 areas, 3 mice per group). **i**, Mean distance of young and old HSCs to the nearest Nes-GFP^{low} cell ($n=94$ young HSCs from 7 areas and $n=135$ old HSCs from 7 areas, 3 mice per group). **j**, **k**, Distance between young and old HSCs to the nearest (**j**) Nes-GFP^{high} cell (137 young HSCs from 9 areas and 275 old HSCs from 12 areas. $n=3$ mice per group) and (**k**) Nes-GFP^{low} cell, (94 young HSCs from 7 areas and 135 old HSCs from 7 areas. $n=3$ mice per group). The experiments in **b**, **f** were repeated three independent times with similar results. Data represent mean ± s.e.m. In **d**, **h**, **i** the statistical significance was assessed by two-tailed Mann-Whitney-test, in **a**, **e**, **j**, **k** the statistical significance was assessed by two-way-ANOVA-test and in **c**, **g** by two-tailed unpaired *t*-tests. Scale bars, 20 µm (**b**); 40 µm (**f**). See also **Source Data** Extended Data Fig. 4.

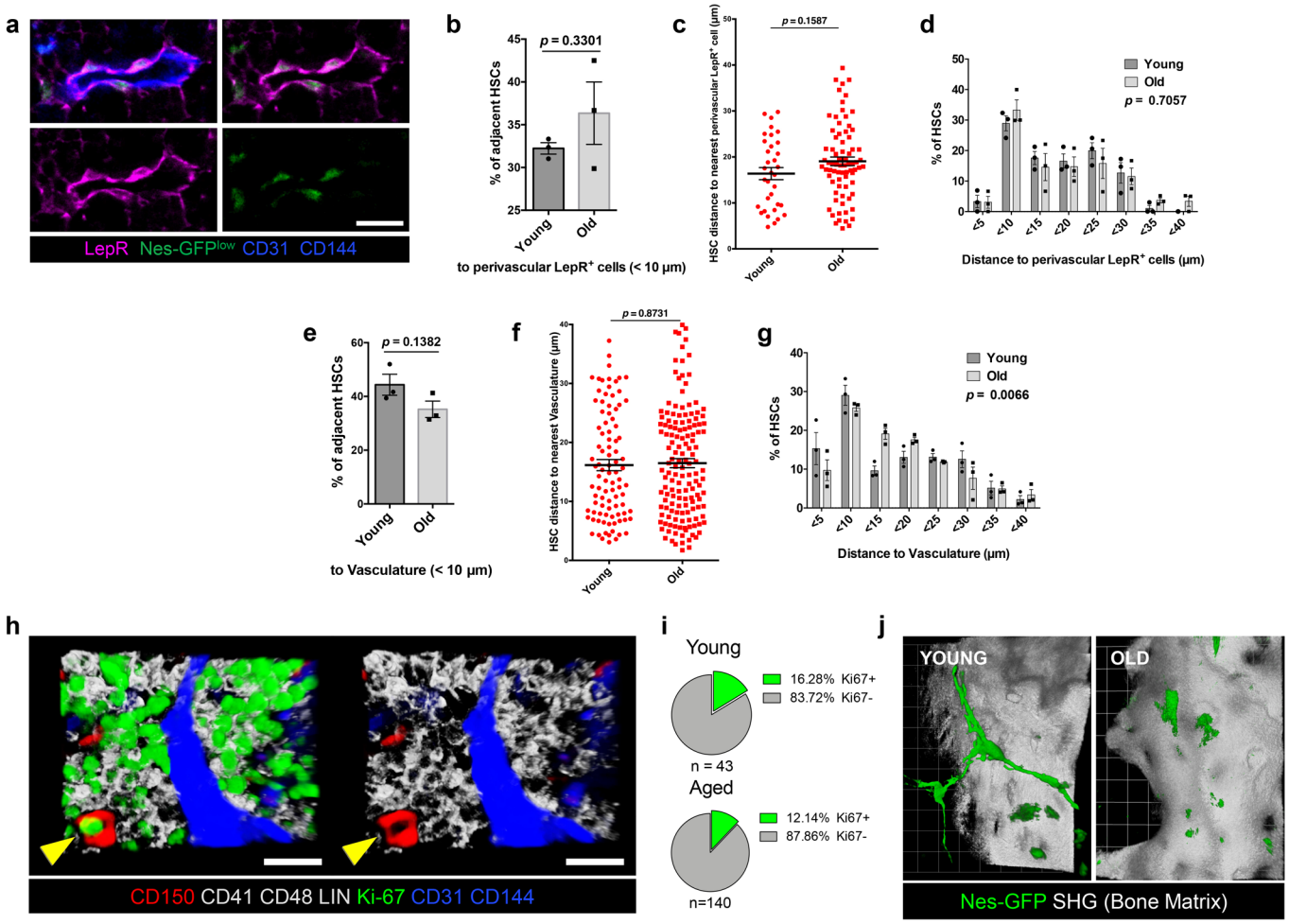

Extended Data Fig. 5 | HSC proximity to LepR$^+$ cells and HSC Ki67 + frequency are not altered upon ageing. **a**, Whole-mount confocal images revealing the overlap of perivascular LepR$^+$ cells (red) and Nes-GFP^{low} cells (green) surrounding sinusoidal vessels (blue) in central BM of Nes-GFP mice. **b**, Percentage of young and old HSCs adjacent to perivascular LepR$^+$ cells (< 10 µm; 96 young HSCs from 12 areas and 147 old HSCs from 12 areas, $n = 3$ femurs and two mice per group). **c**, Mean distance of young and old HSCs to the nearest perivascular LepR$^+$ cells (< 10 µm; $n = 96$ young HSCs from 12 areas and $n = 147$ old HSCs from 12 areas, 3 femurs and two mice per group). **d**, Percentages of young and old HSCs to the nearest perivascular LepR$^+$ cell. (96 young HSCs from 12 areas and 147 old HSCs from 12 areas, $n = 3$ femurs and two mice per group). **e**, Percentage of young and old HSCs in proximity to BM vasculature (< 10 µm; 193 young HSCs and 397 old HSCs, $n = 3$ mice per group). **f**, Mean distance of young and old HSCs to the nearest vasculature ($n = 193$ young HSCs and $n = 397$ old HSCs, 3 mice per group). **g**, Percentages of young and old HSCs to the nearest vasculature (193 young HSCs and 397 old HSCs, $n = 3$ mice per group). **h**, Confocal images of WT old femoral BM. Arrow (yellow) shows Ki-67$^+$ (green) HSC. **i**, Percentage of Ki-67$^+$ and Ki-67$^-$ HSCs (CD150$^+$ CD41$^-$ CD48$^-$ Lin$^-$) present in femoral whole-mount images in BM of WT young and old mice ($n = 43$ young and $n = 140$ old HSCs, 3 mice per group). **j**, 2-photon microscopy images showing Nes-GFP$^+$ cells (green) at the endosteum of young and aged Nes-GFP mouse BM. Bone (collagen, white) depiction was generated with second-harmonic generation microscopy (1 unit = 13.53 µm). Experiments in **a** were repeated two in **h**, **j** three independent times with similar results. Data represent mean ± s.e.m. In **c**, **f** the statistical significance was assessed by two-tailed Mann-Whitney-test, in **d**, **g** the statistical significance was assessed by two-way-ANOVA-test and in **b**, **e** by two-tailed unpaired *t*-tests. Scale bars, 20 µm (**a**, **h**). See also **Source Data** Extended Data Fig. 5.

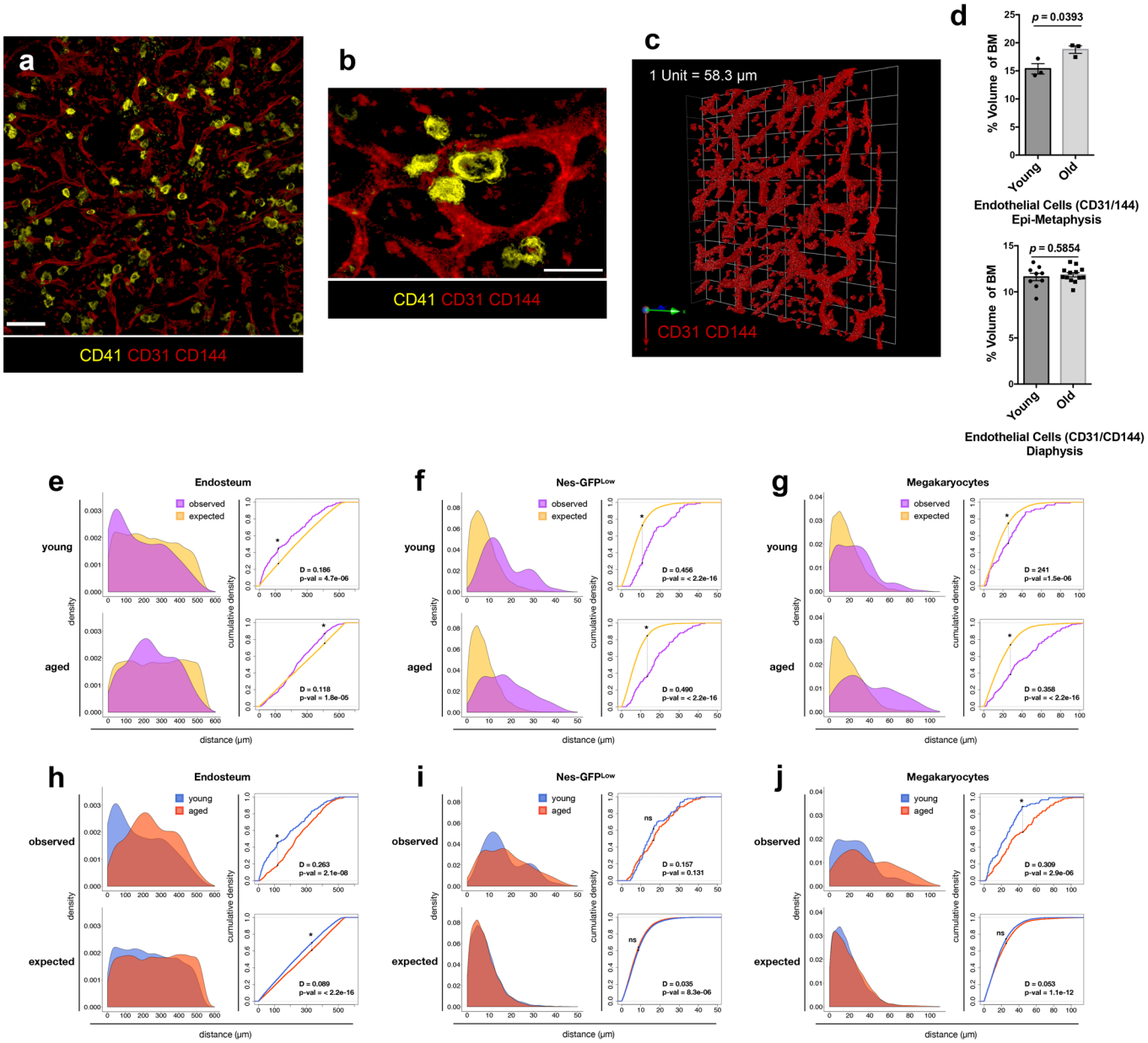

Extended Data Fig. 6 | HSC proximity to selected niche cell types is not random. a, Representative stacked whole-mount images of WT femoral BM showing CD41$^+$ (yellow) MKs and vasculature (red). **b**, Confocal whole-mount image of WT femoral BM showing perisinusoidal CD41$^+$ (yellow) MKs around sinusoids (red). **c**, Representative 3D reconstruction for volume occupancy measurements of CD31$^+$ CD144$^+$ ECs in femoral whole-mount images. **d**, Epiphyseal/metaphyseal and diaphyseal CD31$^+$ CD144$^+$ ECs volume occupancy in young and old long bone BM (upper graph: $n=3$ areas per group, from 3 mice per group; lower graph: young $n=9$ and old $n=13$ areas, from 3 mice per group). The experiments in **a-c** were repeated two independent times with similar results. In **d** data represent mean ± s.e.m and the statistical significance was assessed by two-tailed unpaired *t*-tests. Scale bars, 100 µm (**a**); 20 µm (**b**). **e-g**, Observed (*histology*) and expected (*in silico*) distances of HSCs from endosteum (**e**), Nes-GFP^{low} cells (**f**) or MKs (**g**) in young and aged mice. Statistical differences indicate a non-random distribution of HSCs. **h-j**, Comparison of the distances of HSCs from endosteum (**h**), Nes-GFP^{low} cells (**i**) or MKs (**j**) in young and aged mice according histology (observed young vs observed aged) and *in silico* (expected young vs expected aged) dataset. For **e-j** two-sample Kolmogorov–Smirnov test was used to analyse significance. Alpha levels were selected to control for sample sizes. Observed distance from Nes-GFP^{low} cells: aged: $n=135$ measurements from two maps; young: $n=94$ measurements from two maps. Observed distance from endosteum: aged: $n=432$ measurements from 3 maps; young: $n=192$ measurements from 3 maps. Observed distance from MKs: aged: $n=163$ measurements from 3 maps; young: $n=123$ measurements from two maps. Expected distance from Nes-GFP^{low} cells, endosteum and MKs: aged: $n=10{,}000$ measurements from 3/3/4 maps; young: $n=10{,}000$ measurements from 3/3/5 maps. For further details about the simulation procedure and statistical analysis see *Materials & Methods*. See also Supplementary Figure 1 and **Source Data** Extended Data Fig. 6.

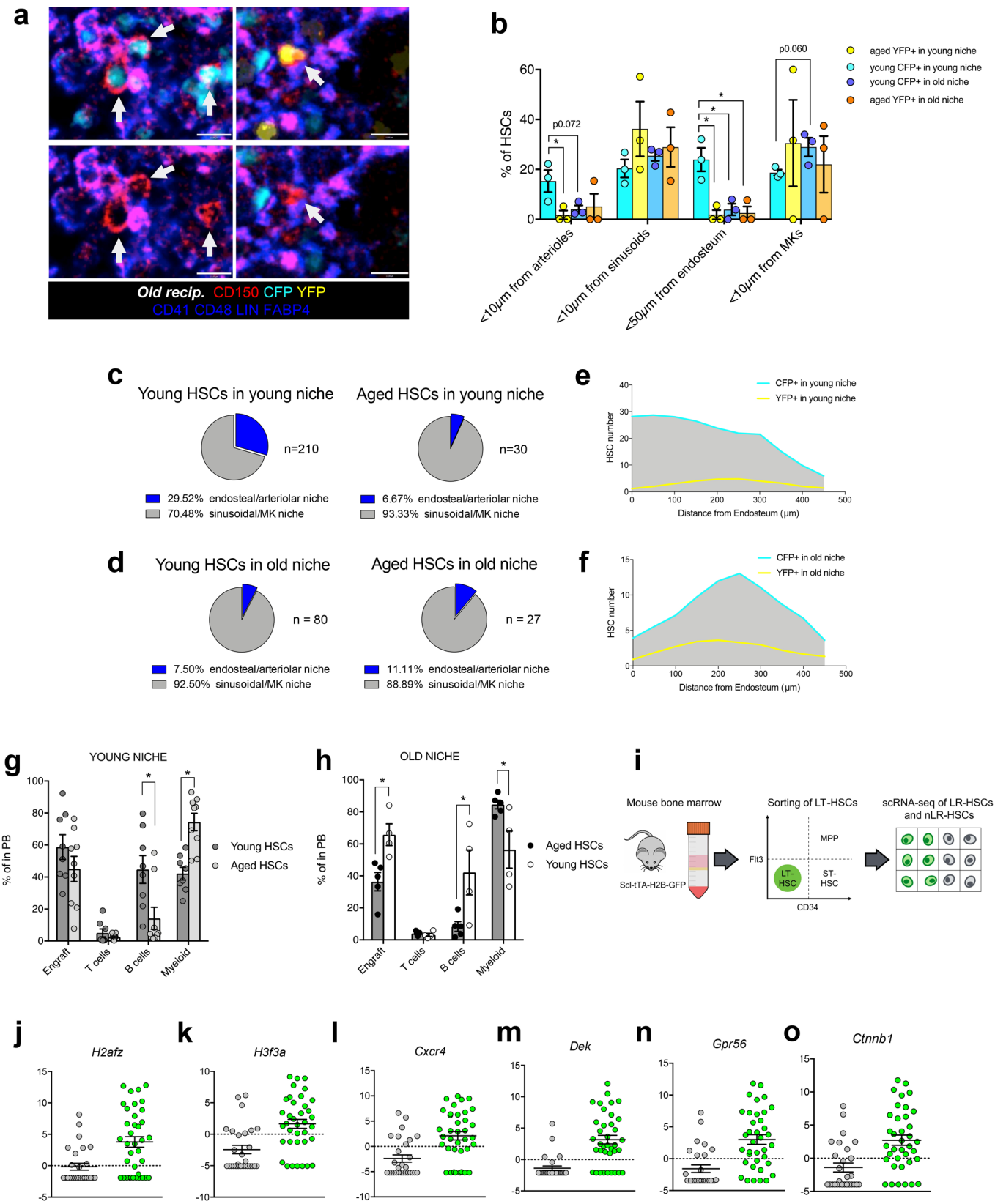

Extended Data Fig. 7 | see next page for caption.

Extended Data Fig. 7 | In young mice, transplanted HSCs lodge in at least two different functional niches, while in the aged the endosteal/arteriolar niche is functionally impaired. a, Confocal images of whole-mount femurs from aged recipient mice transplanted with CFP$^+$ young and YFP$^+$ aged HSCs. Arrows (white) show donor-derived CFP$^+$ young and YFP$^+$ aged HSCs. **b**, Percentage of CFP$^+$ young and YFP$^+$ old HSCs in young and old recipients in proximity to arterioles, sinusoids and megakaryocytes ($<10\,\mu m$) and in the endosteal area ($<50\,\mu m$; $n=3$ young recipient mice with, 210 CFP$^+$ young and 30 YFP$^+$ old HSCs from 31 areas and $n=3$ old recipient mice with 80 CFP$^+$ young and 27 YFP$^+$ old HSCs from 30 areas). **c**, **d**, Percentage of CFP$^+$ young and YFP$^+$ old HSCs in the endosteal/arteriolar and sinusoidal/megakaryocytic niche in young (**c**) and old (**d**) recipients. **e**, **f**, Distribution of CFP$^+$ young and YFP$^+$ old HSCs to the endosteum of young (**e**) and old (**f**) recipients. **g**, **h**, Percentage of engraftment, T cells, B cells and myeloid cells from CFP$^+$ young and YFP$^+$ aged donor HSCs in PB of young recipient (**g**) (young HSCs: $n=8$ mice; aged HSCs: $n=9$ mice) and old recipient mice (**h**) (young HSCs: $n=4$ mice; aged HSCs: $n=5$ mice). **i**, Single cell RNAseq experimental layout. **j-o**, Histone variants (**j**) *H2afz*, (**k**) *H3f3a* and HSC regulators (**l**) *Cxcr4*, (**m**) *Dek*, (**n**) *Gpr56* and (**o**) *Ctnnb1* are upregulated in LR-HSCs. Values related to single cells and referred to DESeq-normalized and baselined log(FPKM). Data are plotted as average population expression ±SD ($n=28$ nLR-HSCs, $n=37$ LR-HSCs). Experiments in **a** were repeated three independent times with similar results. In **b**, **g**, **h** data represent mean ± s.e.m and the statistical significance was assessed by two-tailed unpaired *t*-tests. * $p<0.05$. Scale bars, 10 μm (**a**). See also **Source Data** Extended Data Fig. 7.

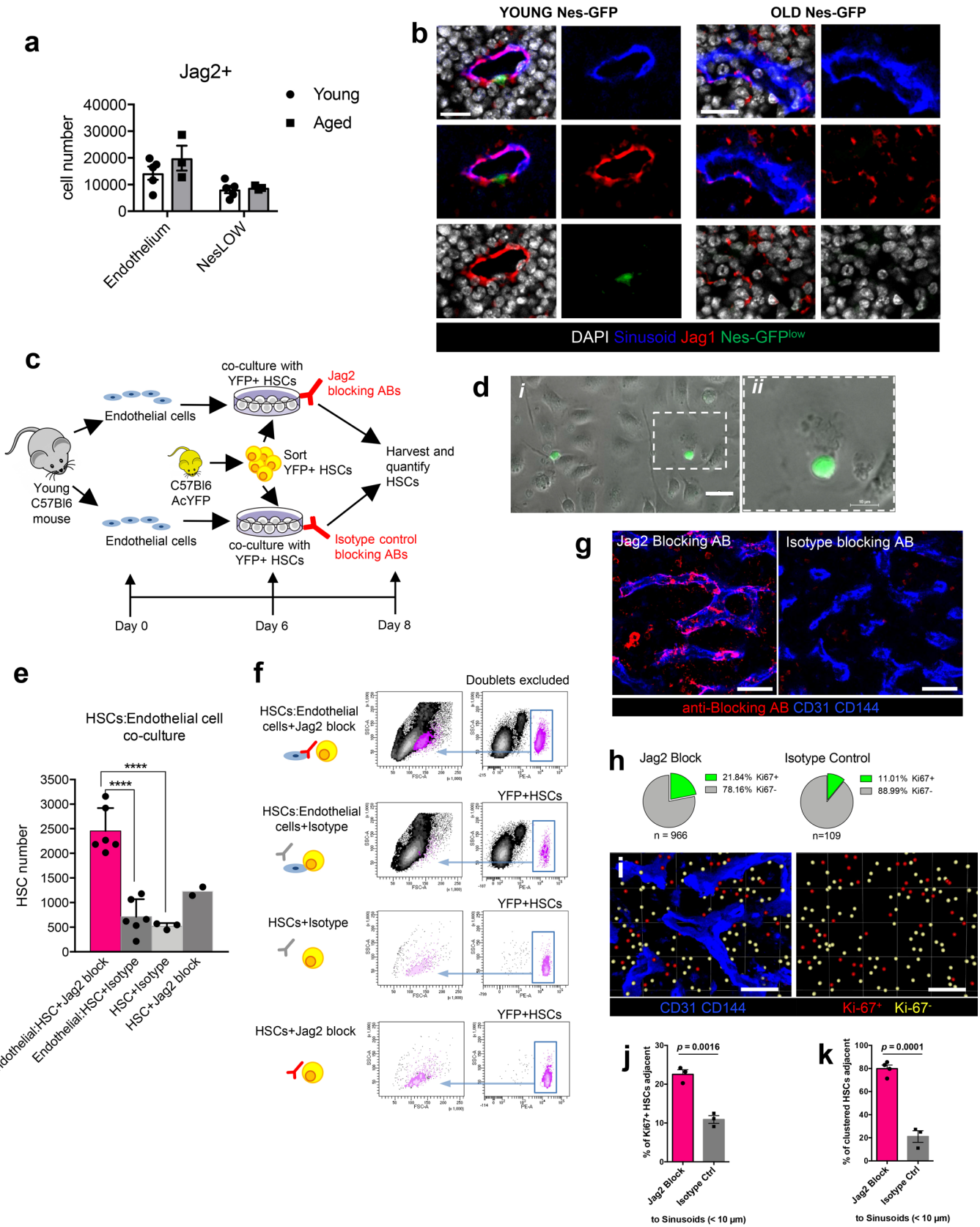

Extended Data Fig. 8 | see next page for caption.

Extended Data Fig. 8 | Endothelial Jag2 maintains aged LR-HSCs at sinusoids. a, Endothelial and Nes-GFP^{low} cells expressing Jag2 in BM of young and old Nes-GFP mice ($n=5$ young, $n=3$ old mice). **b**, Jag1 (red) in sinusoidal vessels (blue) and Nes-GFP^{low} cells (green) in BM from young and old Nes-GFP mice. DAPI (white). **c**, Overview of the *in vitro* co-culture experiments. **d**, Images showing co-culture of YFP$^+$ HSCs (green) and endothelial cells. **e**, Number of YFP$^+$ HSCs after treatment with Jag2 blocking and isotype control antibody. YFP$^+$ HSCs samples were either assayed in co-culture with freshly prepared ECs or alone (n = 6/6/3/2). **f**, Representative FACS dot plots of the gating strategy for YFP$^+$ HSCs *in vitro* co-culture experiments with ECs and Jag2 blocking antibody. **g**, BM image of a mouse treated with Jag2 blocking antibody or isotype control. Samples were stained with the same secondary antibody (red). Vessels are stained with CD31/CD144 (blue). **h**, Percentage of Ki-67$^+$ and Ki-67$^-$ HSCs in distal-diaphyseal-femoral central BM areas of Jag2 blocking antibody and isotype control antibody treated mice (n = 966 and n = 109 HSCs per group from 3 areas per group; 2/3 mice/group). **i**, Representative 3D reconstruction of Ki-67$^+$ (red dots) and Ki-67$^-$ (yellow dots) HSCs at sinusoids in distal-diaphyseal-femoral central BM of Jag2 blocking antibody treated mice. **j-k**, Percentage of Ki-67$^+$ HSCs in proximity to sinusoids (**j**) and of clustered HSCs (**k**) in BM of mice treated with Jag2 blocking antibody and isotype control (**j**, 472 and 28 HSCs from $n=3$ areas per group, 2/3 mice/group; **k**, 653 and 28 HSCs from $n=4$ and $n=3$ areas, 3 mice/group). Experiments in **b**, **d**, **g**, **i** were repeated three, in **f** 6 independent times with similar results. Data represent mean ± s.e.m. In **a**, **j**, **k** the statistical significance was assessed by two-tailed unpaired *t*-tests in **e** by one-way-ANOVA-test. **** $p<0.0001$. Scale bars, 20 μm (**b**, **d***i*), 10 μm (**d***ii*), 50 μm (**g**, **i**). See also **Source Data** Extended Data Fig. 8.

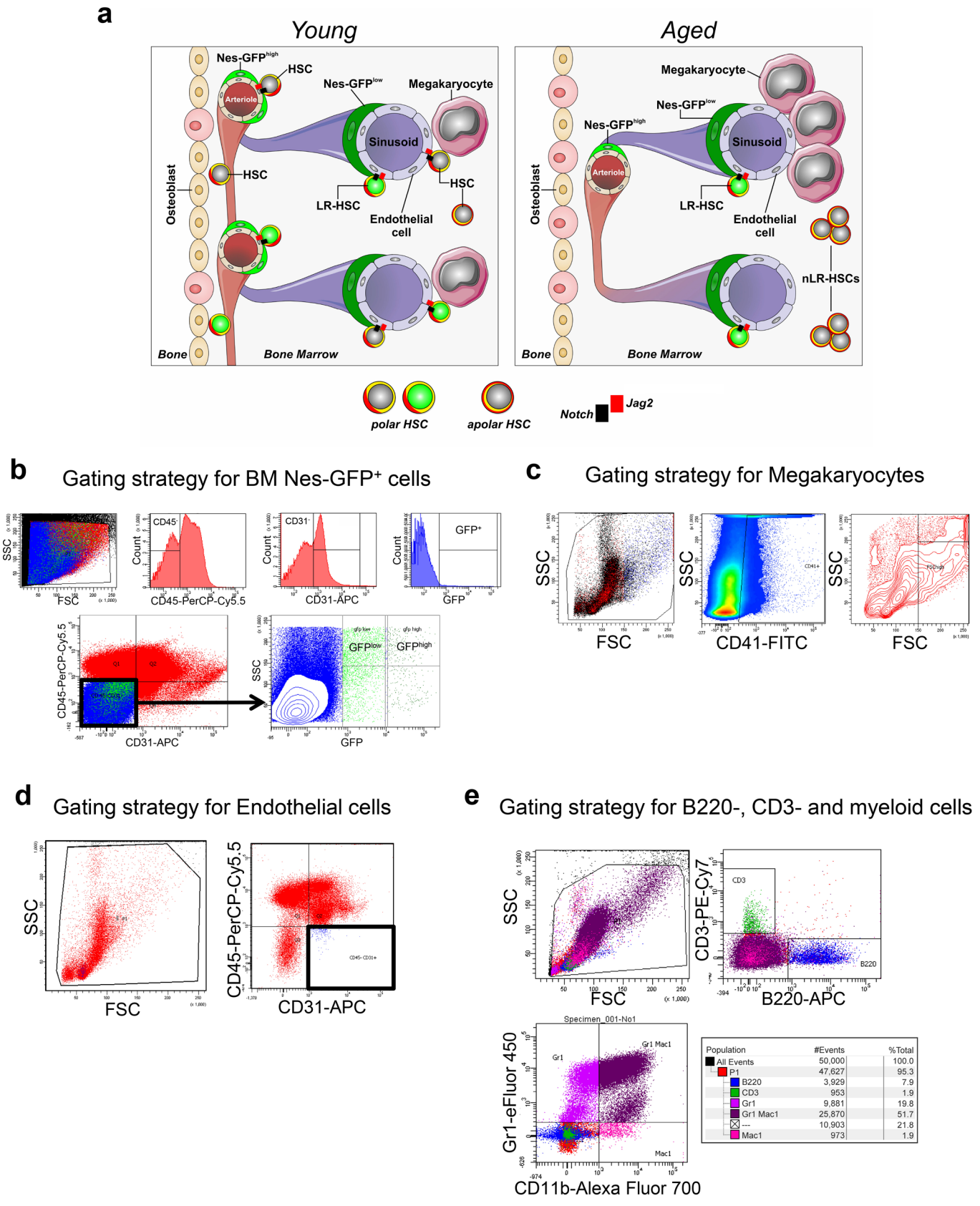

Extended Data Fig. 9 | see next page for caption.

Extended Data Fig. 9 | Impairment of the sinusoidal niche after 5-FU administration. a, Experimental layout. **b**, Young 5-FU treated mice show Ki-67$^+$ (green) CD150$^+$ (red) CD41 CD48 Lin$^+$ (white) clusters of MPPs. **c**, Experimental layout. **d**, Red blood cell count (RBC), myeloid (Gr1$^+$, Mac1$^+$), B cell (B220$^+$) and T cell (Cd3$^+$) frequencies in PB of 5-FU treated young and old mice (Young + 5FU: $n = 7$ mice for each panel; Aged + 5FU: $n = 8$ mice for each panel). **e**, Experimental layout of transplantations of 5-FU preconditioned, lethally irradiated (11 Gy) and control young and aged recipient mice with young or old YFP$^+$ donor HSCs. **f**, Percentage of engraftment from YFP$^+$ HSCs in PB of young and aged control and 5-FU preconditioned recipients ($n = 4/6/4/6$ mice). **g**, BV diameter per volume in stacked images in central BM ($\geq 50\,\mu m$ from endost) from 5-FU treated (30d) and non-treated young and old mice (135/162/151/142 BVs from $n = 3$ areas, two mice per group). **h**, Z-stacked images showing vasculature (CD31/CD144) in bones from young and old mice 30 days after 5-FU administration and non-treated controls. **i**, t-SNE representation of gene expression data of 1218 young and 338 aged CD31$^+$ ECs. **j**, Heatmap of differentially expressed genes. 59 of 1570 genes were deemed significant using DESeq2 (FDR adjusted p-value < 0.1). Color mapping shows log-transformed, size-factor normalized and batch corrected expression. Rows were hierarchically clustered using complete linkage. **k**, Diffusion map representation of cell cycle states of young and aged CD31$^+$ ECs. Cell cycle partitioning was performed based on gene expression data. **l**, Percentage of Ki-67$^+$ and Ki-67$^-$ HSCs in BM images of WT young and old mice 30 days after 5-FU administration ($n = 80$ young HSCs and $n = 156$ old HSCs, 3 mice per group). **m**, Frequency of HSCs and LSKs among BM cells in control and 30-day-5-FU treated young and aged mice ($n = 10/6/9/6$ mice for HSCs, $n = 4/6/4/6$ mice for LSKs). Experiments in **b**, **h** were repeated three independent times with similar results. In **d** the statistical significance was assessed by two-way-ANOVA-test. In **f**, **g**, **m** data represent mean ± s.e.m and statistical significance was assessed by two-tailed unpaired *t*-tests. * $p < 0.05$, ** $p < 0.01$, *** $p < 0.001$. Scale bars, 50 μm (**b**); 100 μm (**h**). The statistical details for **d** are available in **Source Data** Extended Data Fig. 9. See also Supplementary Table 5.

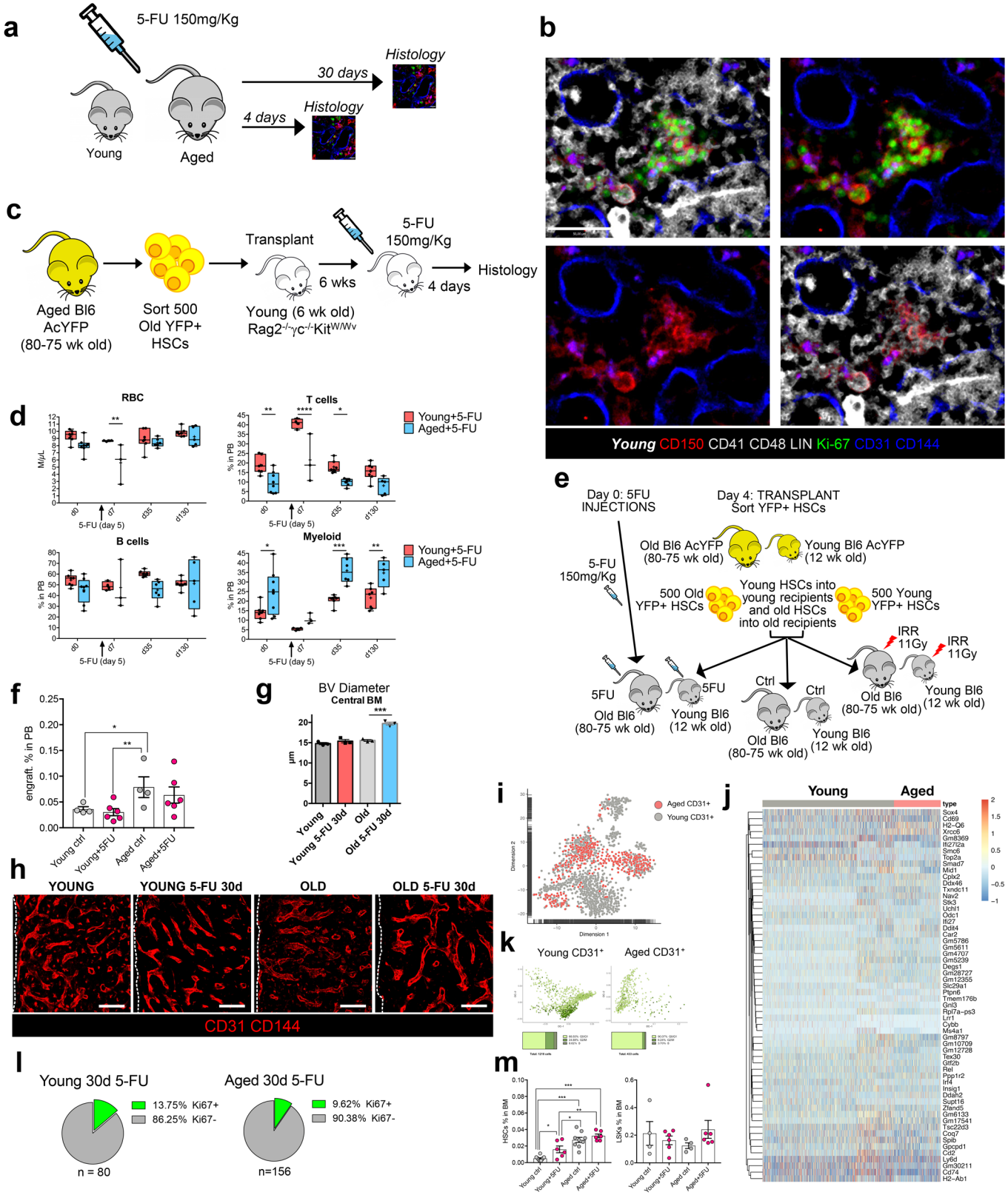

Extended Data Fig. 10 | see next page for caption.

Extended Data Fig. 10 | Summary cartoon scheme and gating strategies. a, Cartoon scheme depicting alterations of the aged niches. Aged HSCs compared to young are located more distant to the endosteum, to megakaryocytes, to arterioles and to periarteriolar Nes-GFP^{high} cells but not to Nes-GFP^{low} cells and sinusoids. With aging megakaryocytes are increased in number. Endosteal endothelial cells and endosteal/periarteriolar Nes-GFP^{high} cells are dramatically reduced. The anatomy and morphology of arteries and arterioles in the aged BM is massively changed. The morphology, anatomy and numbers of central BM vessels, which are comprised mainly of sinusoids, and perisinusoidal Nes-GFP^{low} cells are preserved upon aging. LR-HSCs, which represent in aged mice the population of aged HSCs with the highest regenerative potential, cell polarity and active Notch signalling, were exclusively found as individual stem cells at sinusoidal niches, whereas aged nLR-HSCs are more distant to sinusoids and to other described BM niche cells and show clustering phenotype. Importantly, Jag2 plays a functional role in the maintenance of proximity and quiescence of HSCs at sinusoids. **b**, Representative gating strategy for Nes-GFP ^{high} and ^{low} BM cells; **c**, Gating strategy for megakaryocytes; **d**, Gating strategy for endothelial cells; **e**, Gating strategy for PB cells. Representative gating strategy example of B220, CD3, Mac-1 and Gr-1 staining profile of white blood cells from an aged C57Bl6 mouse (more than 100-week-old).

nature research

Corresponding author(s): Maria Carolina Florian

Last updated by author(s): Sep 20, 2019

Reporting Summary

Nature Research wishes to improve the reproducibility of the work that we publish. This form provides structure for consistency and transparency in reporting. For further information on Nature Research policies, see Authors & Referees and the Editorial Policy Checklist.

Statistics

For all statistical analyses, confirm that the following items are present in the figure legend, table legend, main text, or Methods section.

n/a	Confirmed
☐	☒ The exact sample size (*n*) for each experimental group/condition, given as a discrete number and unit of measurement
☐	☒ A statement on whether measurements were taken from distinct samples or whether the same sample was measured repeatedly
☐	☒ The statistical test(s) used AND whether they are one- or two-sided *Only common tests should be described solely by name; describe more complex techniques in the Methods section.*
☒	☐ A description of all covariates tested
☐	☒ A description of any assumptions or corrections, such as tests of normality and adjustment for multiple comparisons
☐	☒ A full description of the statistical parameters including central tendency (e.g. means) or other basic estimates (e.g. regression coefficient) AND variation (e.g. standard deviation) or associated estimates of uncertainty (e.g. confidence intervals)
☐	☒ For null hypothesis testing, the test statistic (e.g. *F*, *t*, *r*) with confidence intervals, effect sizes, degrees of freedom and *P* value noted *Give P values as exact values whenever suitable.*
☒	☐ For Bayesian analysis, information on the choice of priors and Markov chain Monte Carlo settings
☐	☒ For hierarchical and complex designs, identification of the appropriate level for tests and full reporting of outcomes
☐	☒ Estimates of effect sizes (e.g. Cohen's *d*, Pearson's *r*), indicating how they were calculated

Our web collection on statistics for biologists contains articles on many of the points above.

Software and code

Policy information about availability of computer code

Data collection	Microsoft Office v15.41; BD FACSDiva 8.0.1; Microsoft Office; Zen 2 image analysis software; Volocity (v6.2, Perkin Elmer)
Data analysis	All statistical analyses were determined with Prism 7.0 version. BD FACSDiva 8.0.1; Microsoft Office v15.41; Zen 2 image analysis software; Volocity (v6.2, Perkin Elmer); R-Studio; Cellranger pipeline of 10X Genomics (version 2.1.1); DESeq (v1.22.2, R 3.5.2); edgeR (v3.24.3, R 3.5.2); scater (v1.10.1, R 3.5.2); scran (v1.10.2, R 3.5.2); destiny (v2.12.0, R 3.5.2); M3Drop (v1.8.1, R 3.5.2); ToppGene (toppgene.cchmc.org); ToppCluster (toppcluster.cchmc.org); keras (2.2.4.1); lime (0.4.1). Corel DRAW Graphics Suite X7; Adobe Acrobat Pro DC, Adobe Photoshop CC2019

For manuscripts utilizing custom algorithms or software that are central to the research but not yet described in published literature, software must be made available to editors/reviewers. We strongly encourage code deposition in a community repository (e.g. GitHub). See the Nature Research guidelines for submitting code & software for further information.

Data

Policy information about availability of data

All manuscripts must include a data availability statement. This statement should provide the following information, where applicable:

- Accession codes, unique identifiers, or web links for publicly available datasets
- A list of figures that have associated raw data
- A description of any restrictions on data availability

RNA–seq data that support the findings of this study have been deposited in the Gene Expression Omnibus (GEO) under accession code GSE130299. Previously published sequencing data that were re-analysed here are available under ArrayExpress E-MTAB-4547. All other data supporting the findings of this study are available from the corresponding author on reasonable request.

Field-specific reporting

Please select the one below that is the best fit for your research. If you are not sure, read the appropriate sections before making your selection.

☒ Life sciences ☐ Behavioural & social sciences ☐ Ecological, evolutionary & environmental sciences

For a reference copy of the document with all sections, see nature.com/documents/nr-reporting-summary-flat.pdf

Life sciences study design

All studies must disclose on these points even when the disclosure is negative.

Sample size	In order to choose sample size, we used GraphPad StatMate Software Version 2.0b, estimating a standard deviation between 2 and 8 (depending on the experiment).
Data exclusions	Some of the recipient mice in the transplant experiments were excluded from the final analysis because they failed to meet criteria for engraftment (i.e. contribution to at least 0.1% of total white blood cells in peripheral blood after 20weeks from transplant). Criteria for exclusions were pre-established.
Replication	Experiments were replicated using always the same machines, instruments and softwares for data collection and analysis. quality and robustness of instruments were regularly checked before each experiment. Technical support in sample preparations was also always the same throughout the experiments in the studies. All samples and mice were handled following the same protocols.
Randomization	Samples allocation was random and mice for experiments were randomly chosen.
Blinding	The investigator was not blinded to the mouse group allocation nor when assessing the outcome of experiments (Rag2-/-gammac-/-KitW/Wv mice and aged mice require particular care and follow up).

Reporting for specific materials, systems and methods

We require information from authors about some types of materials, experimental systems and methods used in many studies. Here, indicate whether each material, system or method listed is relevant to your study. If you are not sure if a list item applies to your research, read the appropriate section before selecting a response.

Materials & experimental systems

n/a	Involved in the study
☐	☒ Antibodies
☒	☐ Eukaryotic cell lines
☒	☐ Palaeontology
☐	☒ Animals and other organisms
☒	☐ Human research participants
☒	☐ Clinical data

Methods

n/a	Involved in the study
☒	☐ ChIP-seq
☐	☒ Flow cytometry
☒	☐ MRI-based neuroimaging

Antibodies

Antibodies used	Information about all antibodies used in this study and their validation has been provided in Supplementary Table 6.
Validation	Information about all antibodies used in this study and their validation has been provided in Supplementary Table 6.

Animals and other organisms

Policy information about studies involving animals; ARRIVE guidelines recommended for reporting animal research

Laboratory animals	All C57/Bl6 mice were females and derived from in-house colonies or from commercial suppliers. Nestin-GFP mice were on a C57/BL6 background and were derived by in-house colonies. Rag2-/-gc-/-KitW/Wv mice were derived from in-house colonies. Young C57Bl6 were 10-16 week old. Old C57BL6 mice were 80-110 week old. Young Rag2-/-gc-/-KitW/Wv recipient mice were 5-10 week old. Old Rag2-/-gc-/-KitW/Wv recipient mice were 56-64 week old.
Wild animals	The study didn't involve wild animals
Field-collected samples	The study didn't involve samples collected from the field.

Ethics oversight	All mouse experiments were performed in compliance with the German Law for Welfare 289 of Laboratory Animals and were approved by the Institutional Review Board of the University of Ulm as well as by the Regierungspraesidium Tuebingen (state government of Baden-Württemberg)

Note that full information on the approval of the study protocol must also be provided in the manuscript.

Flow Cytometry

Plots

Confirm that:

☒ The axis labels state the marker and fluorochrome used (e.g. CD4-FITC).

☒ The axis scales are clearly visible. Include numbers along axes only for bottom left plot of group (a 'group' is an analysis of identical markers).

☒ All plots are contour plots with outliers or pseudocolor plots.

☒ A numerical value for number of cells or percentage (with statistics) is provided.

Methodology

Sample preparation	All bone marrow and peripheral blood samples were prepared freshly the same day of the experiment. In the case of peripheral blood samples, after blood collection samples were briefly stored on ice and stained within 1 hour from collection. Flow cytometry analyses were always performed within the following 3-4 hours. The samples were accurately stored on ice in the dark till flow cytometric analysis. As for bone marrow samples, bone marrow was flushed from long bones after the mouse sacrifice and cells were immediately processed for staining. Samples were always stored on ice throughout the procedure. As for histology, bones were also processed immediately after the mouse sacrificed. After fixation, bones were stored at -80°C till the staining. Microscopy analysis was performed immediately after the staining and all images were collected within 24-48 hours from the final staining.
Instrument	BD FACS Aria III and LSRII (BD Bioscience)
Software	BD FACSDiva 8.0.1
Cell population abundance	Cells were not post-sorted. Mostly, cell abundance was microscopically checked: if the sorted cell number was below 100 cells, cells were microscopically counted to verify exact number; if sorted cell number was above 100 cells, samples were microscopically checked for relative equal amount.
Gating strategy	Gating strategy are shown in Extended Data Figures 1 and 8.

☒ Tick this box to confirm that a figure exemplifying the gating strategy is provided in the Supplementary Information.